Measurement of the two-photon excitation cross-section of the 6p'[3/2]2 and 6p'[1/2]0 levels of Xe I at the wavelengths 224.3 and 222.6 nm

C Drag, F Marmuse, Christophe Blondel

Plasma Sources Science and Technology

Measurement of the two-photon excitation cross-section of the $6p'[3/2]_2$ and $6p'[1/2]_0$ levels of Xe I at the wavelengths 224.3 and 222.6 nm

To cite this article before publication: Cyril Drag *et al* 2021 *Plasma Sources Sci. Technol.* in press https://doi.org/10.1088/1361-6595/abfbeb

Measurement of the two-photon excitation cross-section of the $6p'[3/2]_2$ and $6p'[1/2]_0$ levels of Xe I at the wavelengths 224.3 and 222.6 nm

C Drag, F Marmuse and C Blondel

Laboratoire de Physique des plasmas, Centre national de la recherche scientifique, Université Paris-Saclay, Sorbonne Université, Observatoire de Paris, École polytechnique, Institut polytechnique de Paris, route de Saclay, F-91128 Palaiseau, France

E-mail: christophe.blondel@lpp.polytechnique.fr

Abstract.

The two-photon excitation cross-section is a key parameter for the two-photon absorption laser induced fluorescence (TALIF) method, which is commonly used to measure atomic densities in gaseous media, especially for plasma diagnostics. The method consists in recording the fluorescence signal that follows the resonant absorption of two photons of UV light. Calibration often relies on comparing the signal recorded in the studied sample with the fluorescence produced, at a similar wavelength, in a noble gas vapor, the density of which can be easily known. The ratio of the involved cross-sections however plays an essential role for the accuracy of such measurements. Yet the two-photon excitation cross-section of atomic xenon, which is often used as the reference for oxygen density measurements, was measured only once, at the wavelengths of interest. The aim of the present study has been to consolidate the experimental value of that key parameter. The cross-section is found equal to $1.36^{+0.46}_{-0.34}$ and $1.88^{+0.75}_{-0.54} \times 10^{-43}$ m^4 for the $6p'[3/2]_2$ and $6p'[1/2]_0$ levels, respectively. For the $6p'[3/2]_2$ level this is more than twice smaller than previously admitted. Even though the necessarily large relative uncertainty of a non-linear cross-section attaches a relatively large uncertainty to this factor of one half, the result suggests that atomic densities already measured by Xe-calibrated TALIF may have to be revised to significantly lower values. The experiments performed also provide an opportunity to revisit the validity of the approximations used for quantitative TALIF measurements and the collisional broadening and pressure shift of the two-photon $6p'[1/2]_0$ line. A new formula has been used to describe the two-photon absorption of a Gaussian beam in a long gas cell, which makes the decrease of the beam intensity a simple analytic expression even in strong absorption regime, based on a polylogarithmic function of the absorption rate variable.

Submitted to: *Plasma Sources Sci. Technol.*

1. Introduction

1.1. Two-photon absorption laser induced fluorescence (TALIF)

Observing subsequent fluorescence, after an atom has been excited by two-photon absorption, is so natural a detection method that it was actually the one used for the very first experimental demonstration of two-photon excitation, of cesium vapor by a ruby laser (Abella 1962). Once the difficulty raised by the necessity of using an illumination large enough to produce substantial two-photon excitation had been circumvented by the advent of "optical masers", having two photons absorbed in a standing wave also appeared as a convenient method to perform Doppler-free spectroscopy (Vasilenko et al. 1970, Cagnac et al. 1973, Grynberg & Cagnac 1977). Doppler-free two-photon absorption today remains a key method for atomic metrology, including the quest for an explanation of the proton radius puzzle (Fleurbaey et al. 2018).

As concerns detection, TALIF was proposed by several teams as an efficient method to locally detect atomic species, either O (Pindzola 1978, McIlrath et al. 1979), the one or the other isotope of hydrogen (Bokor et al. 1981) or N (Bischel et al. 1981). The same method, when implemented in the two-photon Doppler-free configuration, can also yield information on collisional broadening (Dyer & Crosley 1989).

1.2. Optical diagnostics of gas-phase chemical reactions

Reviews about optical diagnostics of low pressure plasmas can be found in the literature (Dreyfus et al. 1985). TALIF has appeared as a significant technique in that field. It was extended to a wide variety of atoms, including O (Bischel et al. 1982), N (Bischel et al. 1982, Adams & Miller 1998), Cl (Heaven et al. 1982), S (Brewer et al. 1982), C (Das et al. 1983), I (Brewer et al. 1983, Tiee et al. 1983), SH and SD radicals (Tiee et al. 1983), F (Herring et al. 1988), H (Preppernau et al. 1989, Meier et al. 1990, Van der Heijden et al. 2000, Boogaarts et al. 2002), Kr (Whitehead, Cannon & Wacker 1995), Xe (Marchal et al. 2010) and Ar (Matsuta & Kitagawa 2012). Two-photon excitation was also optimized to prepare metastable Kr atoms (Dakka et al. 2018).

1.3. The special case of oxygen, and the different quantitative ways to measure oxygen density

Oxygen has played an important role in many plasma physics experiments, especially plasma-assisted surface chemistry and gas-phase reactions. That motivated many authors to use TALIF to detect O atoms and measure O densities, following the pioneering work of Bischel et al. (1982) (Aldén et al. 1982, DiMauro et al. 1984, Walkup et al. 1986, Goldsmith 1987). More recently, progress in the accuracy of the laser sources made it possible to use TALIF to establish revised values of the first triplet energy levels of oxygen (Marinov et al. 2017).

The straightforward method to deduce the atomic density from the fluorescence signal requires quantitative photometry and a completely calibrated detection chain.

The atomic two-photon generalized cross-section must be known quantitatively in a reliable way. As concerns the most widely used, $2p^4\,{}^3P \rightarrow 2p^3 3p\,{}^3P$, transition in oxygen, the 2-photon generalized cross-section, at the wavelength $\lambda = 226\,\mathrm{nm}$, was measured by Bamford et al. (1987). The obtained value was found to agree with a previously calculated one (Saxon & Eichler 1986), "within their combined uncertainties".

1.4. Calibration with a noble gas

Alternatively, making a parallel TALIF experiment in xenon, the density of which can be measured straightforwardly, offers the possibility of a quantitative measurement with no necessity of absolute laser intensity measurements, provided that the same intensity, or intensities with a well-known ratio can be applied to the one and the other system, so as to keep both of them in an unsaturated regime.

Remarkably enough, the $5p^6\,{}^1S_0 \rightarrow 5p^5 7p[3/2]_2$ transition of Xe I can be excited by the absorption of two photons at the wavelength $\lambda = 225.5\,\mathrm{nm}$, very close to the 226 nm wavelength used for the excitation of oxygen, and excitation can be detected in a similar way by recording the subsequent fluorescence to an intermediate state. Similarity of the excitation wavelengths makes it possible to have the laser deliver the same power, or powers in a well-known ratio, with identical spatial and spectral profiles, alternatively into Xe gas and into the O-containing gaseous system to be analyzed. One can then find the unknown O-density as the product of the Xe density, multiplied by the ratios of the two-photon excitation cross-sections, of the spontaneous emission branching ratios to the observed channels and of the collected fluorescence intensities (Goehlich et al. 1998, Niemi et al. 2001).

Excitation of the $6p'[3/2]_2$ level of Xe I at 224.3 nm, using two photons of $4\,458\,117.8\,\mathrm{m}^{-1}$ to reach its energy $8\,916\,235.6\,\mathrm{m}^{-1}$ (Kramida et al. 2020), was then proposed as an alternative to the $7p[3/2]_2$, as a way to get similar wavelengths not only for the two-photon excitation stage but for the subsequent fluorescence too (Niemi et al. 2005). Since then, TALIF with Xe-calibration has become a routine for oxygen density measurements in plasmas (Uddi et al. 2009, Pendleton et al. 2013, van Gessel et al. 2013, Jiang & Carter 2014, Klochko et al. 2015, Annušová et al. 2018). TALIF via the $6p'[3/2]_2$ level of Xe was also used directly to investigate neutral gas depletion in a helicon reactor (Aanesland et al. 2007). As told by Annušová et al. (2018), however, "continuing work at the Laboratory de Physique des Plasmas on DC discharges suggests that using the value of the ratio determined by Niemi et al. (2005) may overestimate the O atom density by up to a factor of two". Dealing with the calibration of O, H and N TALIF with Xe and Kr, Stancu (2020) also noted some inconsistencies, especially with cross-section ratios, and recommended to revisit the two-photon absorption cross-sections of interest with more precise techniques, especially by direct absorption measurements (Blondel et al. 2020).

Comparative TALIF can also be applied to H and N, the commonly used two-photon excitation wavelengths of which (205 and 207 nm, respectively) happen to be close to a

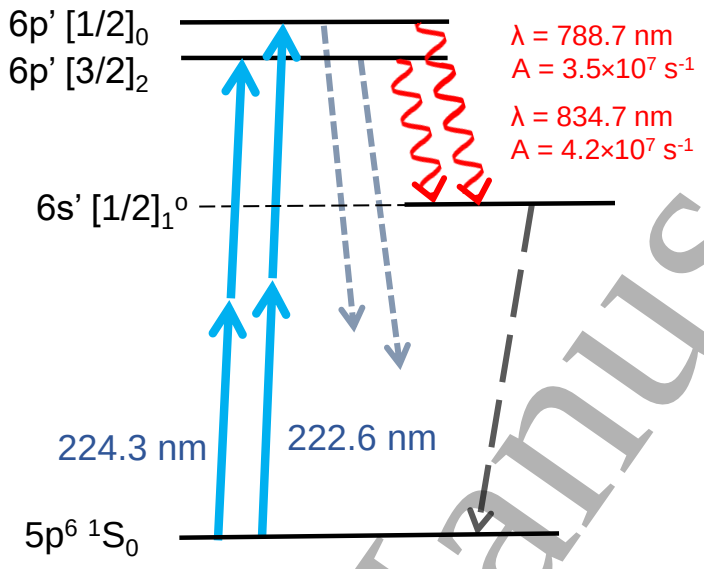

Figure 1. Two-photon excitation paths (continuous arrows) and observed fluorescence (sine arrows) with Einstein coefficient A for the $6p'[3/2]_2$ and $6p'[1/2]_0$ levels of Xe I, the excitation cross-section of which has been measured in the present study (energy levels are not to scale). Dashed arrows show other possible de-excitation paths, including collisional quenching.

serviceable two-photon excitation wavelength of Kr at 204 nm (Niemi et al. 2001). Two-photon excitation of the $5p^5 7f[3/2]_2$ transition of Xe I at 209.3 nm was also proposed as a reference for H measurements, with the advantage of more similar fluorescence wavelengths than with Kr (Elliott et al. 2016). Table 1 shows the state of our knowledge of the two-photon excitation cross-sections of krypton and xenon, and the ratios of these cross-sections to the ones of the species to be measured. A more complete review of the measurements of the two-photon excitation efficiency of the $6p[1/2]_0$, $6p[3/2]_2$ and $6p[5/2]_2$ levels of xenon can be found in Kröll & Bischel (1990), with reference to the work of Chen et al. (1980), Gornik et al. (1981), Pindzola et al. (1981) and Raymond et al. (1984).

As for cross-section ratios in Xe, around 252 nm the cross-section to the $6p[1/2]_0$ level was found 2 to 3 times larger than to the $6p[3/2]_2$, and the cross-section to the $6p[5/2]_2$ was found of the same order of magnitude as the former (Alekseev & Setser 1996). Around 225 nm, the cross-section to the $7p[3/2]_2$ level was found equal to about 0.7 times the cross-section to the $6p'[3/2]_2$. This is a ratio significantly closer to 1 than the maximum ratio of 0.5 (and more likely 0.3) suggested by the Xe vs. O comparisons (see table 1).

Table 1. Most recent data available for integrated 2-photon excitation cross-sections (CS) on noble gases, for different wavelengths (λ). Measurements require calibrated photometry (calibr.) of the measured fluorescence or chemical titration (titr.) of the density of the reactive gas by independent means.

Atom	Top level	λ (nm)	CS (m^4) or CS ratio	Method	Reference
Kr	$6p[3/2]_2$	193.5	$5.4 \times 10^{-45} \pm 50\%$	calibr.	Khambatta et al. (1988)
	$5p[3/2]_2$	214.8	$5.2 \times 10^{-43} \pm 40\%$	calibr.	Dakka et al. (2018)
	$5p'[3/2]_2$	204.2	Kr/H = 0.62 ±50% Kr/N = 0.67 ±50%	titr.	Niemi et al. (2001)
Xe	$7p[3/2]_2$	225.5	Xe/O = 0.36 ± 50% Xe/O = 0.51 ± 50%	titr.	Goehlich et al. (1998)
	$6p'[3/2]_2$	224.3	Xe/O = 1.9 ± 20%	titr.	Niemi et al. (2005)
	$6p[1/2]_0$	249.6	$5.0 \times 10^{-43} \pm 30\%$	calibr.	Kröll & Bischel (1990)
	$6p[3/2]_2$	252.5	$1.7 \times 10^{-43} \pm 30\%$		
	$6p[5/2]_2$	256.0	$2.9 \times 10^{-43} \pm 50\%$		
	$7f[3/2]_2$	209.3	Xe/H = 0.024 ± 54%	Kr comparison	Elliott et al. (2016)

It is clear from this review that the 2-photon excitation cross-section of Xe, especially to the $6p'[3/2]_2$ level, is both a parameter of importance for TALIF measurements of atomic oxygen densities, and still a poorly known quantity. The primary aim of the present work has been to provide a new, independent measurement of this cross-section, to give oxygen-density measurements a better accuracy, in a variety of experimental situations. This also gave an opportunity to make a similar measurement on the $6p'[1/2]_0$ level, the energy of which, 8 986 001.5 m^{-1} (Kramida et al. 2020), less than 1% higher than the energy of the $6p'[3/2]_2$ level, can be reached by absorption of two photons at wavelength 222.6 nm. The $6p'[1/2]_0$ was used, together with the $6p'[3/2]_2$ level, for TALIF diagnostics of atomic densities in the plume of an ion thruster (Eichhorn et al. 2011). Its two-photon excitation cross-section was found to be about 1.2 times the cross-section of the $6p'[3/2]_2$ (Alekseev & Setser 1996) †. Being a $J = 0$ level, the $6p'[1/2]_0$ offers the advantage of having no hyperfine structure. Excitation and de-excitation schemes for both levels are presented on figure 1.

†Eichhorn et al. (2011) find a factor 1.1, but with "an uncertainty factor 2-3".

2. Theory

2.1. Cross-section measurement in a macroscopic sample

The reverse measurement of a photoexcitation cross-section, in a gas with a known density, encounters experimental difficulties quite similar to those of TALIF density measurements, which have been described in paragraphs 1.3 and 1.4. Using the fluorescence signal in a quantitative way still requires complete calibration of the detection system. Cross-section ratios may be more easily determined, but if the measured ratio is not directly the one to be used in subsequent density diagnostics, that will add one more variable to the problem, hence one more source of uncertainty to the final measurement.

Some of the difficulties of quantitative fluorescence calibration (including the uncertainty on the branching ratios to different de-excitation channels) can be circumvented by measuring the *absorption* of the laser, after it has passed through a finite-length absorption cell. Precise absorption measurements have to cope with specific difficulties however, particularly because absorption is not a quantity measured with respect to a zero background, but the decrease of a possibly noisy transmission signal. Too low an absorption will make it undetectable against fluctuations of the incident beam intensity, too high an absorption will leave only little signal, with again a dominant relative noise. The optical thickness of the cell has thus to be chosen to give the attenuation factor an intermediate order of magnitude, typically between 10 and 70 % on the axis of the laser beam (where non-linear absorption has its maximum efficiency), at the top of the resonance line. For such attenuation factors, and even more with optical non-linear processes, attenuation does not grow linearly with the thickness of the absorbing cell, nor is it the same all across a laser beam the intensity of which has, by necessity, strong transverse spatial variations. Specific models have thus to be developed to describe how a laser pulse gets attenuated after crossing a macroscopic gas cell, including the case of an optically thick absorbing cell. Establishing such specific models makes it necessary to go back to the basics of two-photon absorption.

2.2. The optical Bloch equations for two-photon excitation

As has been known for decades (Takatsuji 1975, Grischkowsky et al. 1975), two-photon excitation from an atomic ground state $|g\rangle$ of energy $\hbar\omega_g$ to an excited state $|e\rangle$ of energy $\hbar\omega_e$, in the absence of intermediate resonant states, can be modeled as the excitation of a two-level system, with a coupling frequency

$$\Omega = \frac{\mathcal{E}^2}{2\hbar^2}\left|\sum_q \frac{d_{eq}d_{qg}}{\omega_q - \omega_g - \omega}\right| \tag{1}$$

with $\mathcal{E}$ the amplitude of the electric field, ω its angular frequency, d_{eq} and d_{qg} the appropriate electric dipole elements, given the field polarization. The sum over q runs over all possible intermediate states $|q\rangle$, of energy $\hbar\omega_q$. Provided that no intermediate

state ω_q lies too close to the medium energy $(\omega_g + \omega_e)/2$, the coupling frequency $\Omega(\omega)$ may be considered as constant, over the width of the two-photon resonance.

Rigorous reduction of the evolution of the atomic system to that of a two-level atom also shows that the two-photon resonance undergoes a frequency shift with respect to the weak-field condition $2\omega = \omega_e - \omega_g$, which can be viewed as a shift of both the ground and excited states $|g\rangle$ and $|e\rangle$ by angular frequencies

$$\Delta_{g,e} = \frac{\mathcal{E}^2}{2\hbar^2} \sum_q \left| d_{(g,e)q} \right|^2 \left(\frac{1}{\omega_{g,e} - \omega_q - \omega} + \frac{1}{\omega_{g,e} - \omega_q + \omega} \right) \tag{2}$$

respectively, with $\omega \simeq (\omega_e - \omega_g)/2 = \omega_0$.

The coupling frequency Ω and frequency shifts $\Delta_{g,e}$ are not given by identical formulae (with the former depending, among other features, on products of dipole matrix elements and the latter on squared moduli). Formulae (1) and (2) show, however, that, except for special cases, Ω and $\Delta_{g,e}$ can be expected to have similar orders of magnitude.

Within this framework, evolution of the atomic system is described by the optical Bloch equations (OBE) (Takatsuji 1975, Grischkowsky et al. 1975, Allen & Stroud Jr 1982). The two-level system tends towards a stationary solution, either in an underdamped or overdamped regime, depending on the relative magnitude of the coupling frequency Ω, the de-excitation rate Γ of the excited state, the damping rate β of the atomic coherences (which is at least $\Gamma/2$) and the detuning of the excitation with respect to the atomic transition $\delta = 2(\omega - \omega_0)$.†

Regarding the atomic populations, the stationary solution is‡

$$\overline{\rho_{ee}} = \frac{1}{2} \frac{\beta\Omega^2/\Gamma}{\delta^2 + \beta\left(\beta + \Omega^2/\Gamma\right)} \tag{3}$$

If the excitation is applied for a sufficiently long time, the population ρ_{ee} of the excited state $|e\rangle$ eventually stabilizes at the stationary value, which follows a Lorentz distribution as a function of the excitation frequency ω. The two-photon resonance gets spectrally broadened by saturation effects when Ω^2 gets greater than $\beta\Gamma$. At lower intensities, the width of the resonance remains simply equal to twice the damping rate β of the coherences, on a 2ω scale.

2.3. The rate equation regime and the generalized cross-section

When coherences are damped effectively enough, i.e. when both $\beta \gg \Omega$ and $\beta \gg \tau^{-1}$ (with τ the interaction time or laser pulse characteristic duration, such as the τ parameter of a Gaussian time-profile e^{-t^2/τ^2}), coherences can be assumed to adapt

†Overdamping occurs if the discriminant of the cubic equation that gives the eigenfrequencies of the two-level populations and coherences is positive. Explicitly: $-4\Omega^6 - \left[12\delta^2 - (\beta - \Gamma)^2\right]\Omega^4 - 4\delta^2\left[3\delta^2 - 5(\beta - \Gamma)^2\right]\Omega^2 - 4\delta^2\left[\delta^2 + (\beta - \Gamma)^2\right]^2 > 0$. The negative leading term proportional to Ω^6 makes it conspicuous that underdamping, i.e. Rabi oscillations, will always occur at large enough intensities.

‡This is formula (35) of Settersten & Linne (2002).

themselves quasi-instantaneously to the atomic populations; $\rho_{ee}(t)$ can be considered as ruled by a single rate equation (RE), the three terms of which describe excitation from the ground state, stimulated and spontaneous de-excitation from the excited state, respectively:

$$\dot{\rho}_{ee} = -\dot{\rho}_{gg} = -T_{g\leftrightarrow e}(\rho_{ee} - \rho_{gg}) - \Gamma\rho_{ee} \tag{4}$$

with ρ_{gg} the population of the ground state $|g\rangle$. Despite the fact equation (4) is only a first-order one, the stationary limit $\overline{\rho_{ee}}$ of $\rho_{ee}(t)$ is the same as given by (3), provided that the excitation rate $T_{g\leftrightarrow e}$ has been defined as†

$$T_{g\leftrightarrow e} = \frac{\beta\Omega^2}{2\left(\delta^2+\beta^2\right)} \tag{5}$$

In the RE regime, light-induced evolution is thus reduced to direct and equal $|g\rangle \rightarrow |e\rangle$ and $|e\rangle \rightarrow |g\rangle$ pumping rates, proportional to the square of the two-photon coupling frequency Ω. Using equation (1) and the proportionality between the squared amplitude of the exciting field $\mathcal{E}$ and the photon flux Φ, one can formulate the pumping rate $T_{g\leftrightarrow e}$ in a more compact way, introducing a generalized two-photon cross-section $\sigma^{(2)}_{g\leftrightarrow e}$:

$$T_{g\leftrightarrow e} = \sigma^{(2)}_{g\leftrightarrow e}(\omega) \times \Phi^2 \tag{6}$$

with

$$\sigma^{(2)}_{g\leftrightarrow e}(\omega) = \frac{\beta}{2\left(\delta^2+\beta^2\right)} \times \frac{\omega^2}{\left(\epsilon_0\hbar c\right)^2}\left|\sum_q \frac{d_{eq}d_{qg}}{\omega_q - \omega_g - \omega}\right|^2 \tag{7}$$

In the case of broadband excitation, or when the experimentally accessible quantity results from scanning through a possibly broadened resonance, a more relevant quantity is the frequency-integrated cross-section‡

$$\bar{\sigma}^{(2)} = \int \sigma^{(2)}(\omega)\, 2d\omega \tag{8}$$

From (7), the integrated cross-section gets a simple expression§

$$\bar{\sigma}^{(2)} = \frac{\pi}{2}\frac{\omega^2}{\left(\epsilon_0\hbar c\right)^2}\left|\sum_q \frac{d_{eq}d_{qg}}{\omega_q - \omega_g - \omega}\right|^2 = 8\pi^3\alpha^2\frac{\omega^2}{e^4}\left|\sum_q \frac{d_{eq}d_{qg}}{\omega_q - \omega_g - \omega}\right|^2 \tag{9}$$

†This is formula 7.4 of Milonni & Eberly (1978).

‡The commonly, even though not so often explicitly, admitted convention is to make the integration on variable 2ω, which is consistent with the definition of δ as the detuning of the available two-photon energy 2ω with respect to the atomic transition frequency $2\omega_0$ (Bamford et al. 1986, Kröll & Bischel 1990).

§This is formula (1) of Khambatta et al. (1988), formula (4) of Saxon & Eichler (1986), formula (2) of Bamford, Saxon, Jusinski, Buck & Bischel (1988) and the formula given in their appendix by Goehlich et al. (1998). It is analogous to the one-photon formula $\bar{\sigma}^{(1)} = \pi\frac{\omega}{\epsilon_0\hbar c}\left|d_{eg}\right|^2 = 4\pi^2\,\alpha\,\frac{\omega}{e^2}\,\left|d_{eg}\right|^2$.

with e the elementary charge and α the fine structure constant. The latter form makes it more conspicuous that the process is a second-order one with respect to the electromagnetic interaction and that $\bar{\sigma}^{(2)}$ has the dimension of a length to a power of 4.

Conversely, the frequency-dependent cross-section $\sigma^{(2)}(\omega)$ can be regarded as the distribution of the total cross-section $\bar{\sigma}^{(2)}$ on the resonance profile: $\sigma^{(2)}(\omega) = \bar{\sigma}^{(2)} \times g(\omega)$, with a distribution just given by

$$g(\omega) = \frac{\pi^{-1}\beta}{\delta^2 + \beta^2} = \frac{\pi^{-1}\beta}{(2\omega - \omega_e + \omega_g)^2 + \beta^2} \tag{10}$$

Comparing equations (1) and (9), one gets a relation between the integrated cross-section and the proportionality coefficient between the transition rate Ω and the fourth power of the electric field. The relation between $\bar{\sigma}^{(2)}$, Ω and Φ appears very simple†:

$$\bar{\sigma}^{(2)} = 2\pi \frac{\hbar^2\omega^2}{(\epsilon_0 c)^2} \frac{\Omega^2}{\mathcal{E}^4} = \frac{\pi}{2} \frac{\Omega^2}{\Phi^2} \qquad \text{or, equivalently,} \qquad \Omega = \sqrt{\frac{2\bar{\sigma}^{(2)}}{\pi}}\, \Phi \tag{11}$$

2.4. Validity of the rate equation in special cases

2.4.1. Short pulses. Remarkably enough, the RE (4) still makes it possible to calculate an excited population even for short pulse excitation, i.e. when damping can be considered negligible, in the low-excitation regime, provided that the damping rate β is replaced by twice the inverse of the laser pulse duration τ (this has some consistency with the fact that, in such a situation, the resonance experimentally appears broadened, on a frequency scale, by a quantity proportional to $1/\tau$). On the one hand Rabi oscillation at frequency $(\Omega^2 + \delta^2)^{1/2}$, starting from the atomic ground state, builds an excited population that takes off as a quadratic function of interaction time τ: $\rho_{ee}(\tau) \sim \Omega^2\tau^2/4$. On the other hand, according to (5), steady resonant excitation at the rate $\beta^{-1}\Omega^2/2$ would build a population proportional to the interaction time τ, such as $\rho_{ee}(\tau) \sim \beta^{-1}\Omega^2\tau/2$. The lowest-order effect thus appears the same if one damps the rate-equation resonance by $\beta = 2/\tau$. This 'finite-time damping' assumption seemingly extends the validity of the RE to the regime of short pulse excitation, provided that the excited population remains small. Equality happens, however, only for a pulse with constant amplitude Ω, after a clear-cut interaction time τ. Even though the qualitative interpretation may appear tentative, quantitative analysis with rate equations, in the case of short pulses with realistic time-profiles, obviously remains very risky.

2.4.2. Multimode vs. single-mode lasers. With long laser pulses, a conservative recipe has been that "[rate equations] produce reasonable estimate of the excitation fraction for strong excitation only when relaxation processes occur on time scales much shorter than the laser pulse width" (Settersten & Linne 2002), which, in practice, requires pulse

†This is formula (2) of Dakka et al. (2018), after formula (6) of Bamford, Hickman, Dyer & Bischel (1988).

durations of at least a few ns. Matching this criterion does not however prevent optical nutation and free-induction decay to occur for high enough excitation amplitudes, in a manner comparable to what can be observed with one-photon transitions (Loy 1976). Two conditions have thus to be met to make the description by a RE fully realistic: the total relaxation rate, as given by the sum of the atomic relaxation rate and the laser bandwidth, for multimode lasers, must be greater than both the Rabi frequency and the inverse of the pulse duration (Allen et al. 1982, Eagles et al. 1982, Stancu 2020).

The kind of laser we use, however, is not a multimode, but an injection-seeded single-mode laser, which deprives us from a usually very effective damping factor. Atomic collisions, on the other hand, can still contribute to population relaxation and, even more efficiently, to relaxation of the atomic coherences. The kinematics of the atomic absorption has thus to be re-examined in the very conditions of our experiments.

2.5. The quasi-static approximation

As far as it is valid, the rate equation (4) can as well be written

$$T_{g\leftrightarrow e}(\rho_{gg} - \rho_{ee}) = \Gamma\rho_{ee} + \dot{\rho}_{ee} \tag{12}$$

The latter form makes it conspicuous that the net power absorbed from the laser sustains two physical effects: one is the spontaneous energy dissipation from the excited state and the other is the variation of the energy stored in the excited atomic population. Formula (12) can be used to calculate the instantaneously absorbed power $p_{\rm abs}$ whatever model is used, either from the solution of the OBE or from the RE, as

$$p_{\rm abs} = 2\,\hbar\omega \times (\Gamma\rho_{ee} + \dot{\rho}_{ee}) \tag{13}$$

with a factor of 2 made necessary by the fact that two laser photons are absorbed per atomic transition. If one gets only interested at the total energy absorbed when the laser pulse has passed and the atom has got back to its ground state, since $\int \dot{\rho}_{ee}(t)dt = \rho_{ee}(\text{final}) - \rho_{ee}(\text{initial}) = 0$, one can drop the $\dot{\rho}_{ee}$ term and keep only the dissipative term $\overline{p}_{\rm abs} = 2\,\hbar\omega \times \Gamma\rho_{ee}$ of the instantaneously absorbed power. The complete expression, however, remains necessary as long as an energetically consistent description of the system evolution is desired. Under this reservation, if one assumes, in a quasi-static (QS) approximation, that the population ρ_{ee} adapts instantaneously to its stationary value $\overline{\rho_{ee}}$, the power lost by the exciting light can be calculated as the time integral of

$$\overline{p}_{\rm abs}(t) = 2\,\hbar\omega \times \Gamma\ \overline{\rho_{ee}}(t) = \hbar\omega \times \frac{\beta\Omega^2}{\delta^2 + \beta\,(\beta + \Omega^2/\Gamma)} \tag{14}$$

or equivalently

$$\overline{p}_{\rm abs}(t) = 2\,\hbar\omega \times \frac{\Gamma\,\sigma^{(2)}(\omega)\,\Phi^2(t)}{\Gamma + 2\sigma^{(2)}(\omega)\,\Phi^2(t)} \tag{15}$$

2.6. The low-intensity regime

As made conspicuous by formula (15), the QS approximation is still not enough to write the instantaneously absorbed power as the product of the photon flux squared by the generalized cross section. Another, final, approximation is necessary, to neglect the flux-dependent term in the denominator. This is justified when most of the atomic population remains in the ground state, which makes the power given back to the laser by stimulated emission negligible with respect to the absorbed power $2\hbar\omega T_{g\leftrightarrow e}$. Under this condition, formula (15) can be simplified into

$$\overline{p}_{\mathrm{abs}}(t) \simeq 2\,\hbar\omega \times \sigma^{(2)}(\omega)\,\Phi^2(t) \tag{16}$$

which can be used as an alternative definition of the two-photon absorption cross-section, in a low excitation (LE) regime.

Equation (16) serves as the basis for most quantitative TALIF analyses. Before we make it ours in turn, it is worth comparing its output with what the more rigorous OBE, or RE predict for instantaneous absorption. For that purpose, the orders of magnitude involved in our experiment are examined below.

2.7. Orders of magnitude

Typical orders of magnitude, relevant for our TALIF experiments on xenon, are given in table 2. The laser pulse energy, typically 0.5 mJ, can be up to 1 mJ in a minority of experiments.

With a maximum value of Ω significantly larger than Γ, the experiments carried out with the highest laser pulse energies belong to a domain where spontaneous emission would not be enough to reduce the evolution of an isolated atom to a simple RE, like (4).

The experiment however takes place at pressures where collisions can induce substantial de-excitation of the $6p'[3/2]_2$ (resp. $6p'[1/2]_0$) level at a rate proportional to the density n of the xenon vapor, with a coefficient $k_Q = 4.26(10) \times 10^{-16}\,\mathrm{m^3 s^{-1}}$ (resp. $4.23(8) \times 10^{-16}\,\mathrm{m^3 s^{-1}}$) (Bruce et al. 1990, Whitehead, Pournasr, Bruce, Cai, Kohel, Layne & Keto 1995). Collisional de-excitation is thus expected to dominate, as soon as the xenon pressure gets higher than 300 Pa. Moreover atomic coherences can be perturbed by elastic collisions even though, by definition, these collisions do not change the populations, so β can be increased, due to pressure effects, by a still higher rate.

Most data presented in the present work have been acquired with pressures between 1000 and 10^4 Pa. Figures 2 and 3 show what happens at the lower pressure, for the resonant instantaneous absorption and the frequency-dependent time-integrated absorption, respectively, by one atom. Characteristic times, at that pressure (which corresponds to an atom density of about $2.4 \times 10^{23}\,\mathrm{m^{-3}}$), have critically similar orders of magnitude: the excited-level lifetime $1/\left(\Gamma + Qn\right)$ reduces to about 7.6 ns, not much bigger than the pulse characteristic duration $\tau = 6\,\mathrm{ns}$, and the inverse of the coupling

Table 2. Typical parameter values in the present 2-photon excitation experiment, including the maximum value of the normalized Doppler broadening factor (at 300 K), which determines the peak value of the effective cross-section. The case chosen is the one of $6p'[1/2]_0$ excitation.

Quantity	Symbol	Value	Unit
Laser waist	w	440	μm
Pulse energy	E	0.5	mJ
Pulse characteristic duration	τ	6	ns
Peak intensity	I	1.5×10^{11}	$\mathrm{W/m^2}$
Wavelength	λ	222.6	nm
Photon energy	$\hbar\omega$	8.92×10^{-19}	J
Peak photon flux	Φ_0	1.7×10^{29}	$\mathrm{m^{-2}\,s^{-1}}$
Integrated cross-section	$\bar{\sigma}^{(2)}$	1.8×10^{-43}	$\mathrm{m^4}$
Peak resonant Rabi frequency	Ω	5.9×10^{7}	$\mathrm{rad\,s^{-1}}$
Spontaneous emission rate	Γ	2.9×10^{7}	$\mathrm{s^{-1}}$
Coherence damping rate	$\beta \geq \Gamma/2$	1.5×10^{7}	$\mathrm{s^{-1}}$
Resonant cross-section	$\sigma^{(2)}(0)$	3.9×10^{-51}	$\mathrm{m^4\,s}$
Doppler distribution max. ($2\omega = 0$)	$D(0)$	5.1×10^{-11}	s
Max. effective cross-section	$\sigma_{\mathrm{D}}^{(2)}(0)$	9.2×10^{-54}	$\mathrm{m^4\,s}$
Atom density	n	10^{24}	$\mathrm{m^{-3}}$
Collisional de-excitation coefficient	k_Q	4.2×10^{-16}	$\mathrm{m^3\,s^{-1}}$
Cell length	z	0.51	m

frequency Ω, at the peak of a 1 mJ pulse, is such that $\Omega^{-1} \simeq 8.5\,\mathrm{ns}$. Without any possibility to assume one time significantly smaller or greater than another, no wonder that all four models, OBE, RE, QS and the LE model tell different stories. Furthermore the differences are not just in the timing of the absorbed power. Even after time-integration, resonant absorption remains strongly dependent on the model used, as shown by the different positions of the points of zero abscissa in figure 3. At the lower pressure of 100 Pa, the absorption would even be greater by 20% with the OBE than with the RE, whereas the QS model would underestimate this energy by nearly a factor of 2. At the pressure of 1000 Pa, the discrepancies are not necessarily reduced by using lower energy pulses, since the OBE and RE models still disagree by a factor of 2 (albeit inversed) when the pulse energy is reduced to $2 \times 10^{-4}\,\mathrm{J}$. Fortunately, the increased damping given by still higher pressures effectively brings all models together. Raising the pressure to 15000 Pa, without any additional damping of the atomic coherences (the elastic collisional damping of which is unknown), one can reconcile all four models within $\pm 1.5\,\%$. A paradoxical result of these calculations may thus be that, in the present experiment, data taken at higher pressures finally appear more reliable.

However, the discrepancies between the OBE, RE, QS and LE predictions can be efficiently reduced, as suggested by figure 3, when absorption is integrated on the whole spectral width of the atomic resonance. In spite of the fact that time-integrated absorption may exhibit macroscopic differences at given frequencies, the frequency

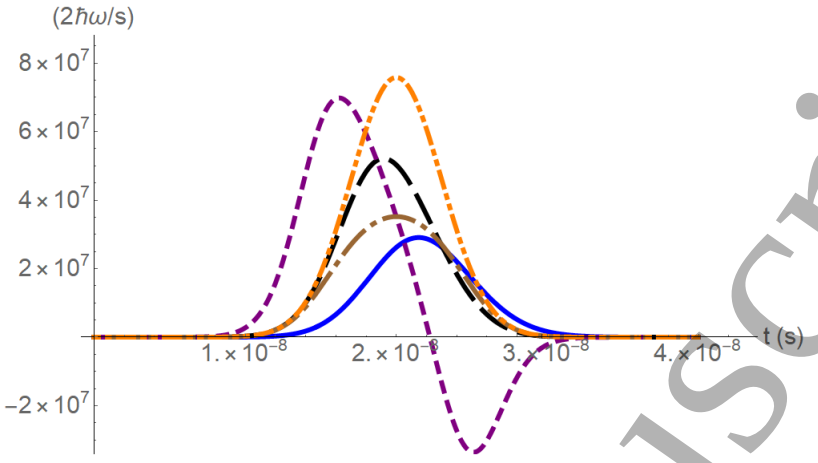

Figure 2. Instantaneous absorption rate $p_{\rm abs}(t)$ by one atom, according to different models, in units of $2\,\hbar\omega/\mathrm{s}$, as a function of time (s), for a laser pulse of 1 mJ, assuming a Gaussian time-profile with a characteristic duration $\tau = 6\,\mathrm{ns}$ arbitrarily centered at time $t = 20\,\mathrm{ns}$, zero detuning ($\delta = 0$) with respect to the $6p'[1/2]_0$ resonance, waists $w_x = w_y = 440\,\mu\mathrm{m}$ and a Xe pressure of 1000 Pa that induces a total de-excitation rate of $1.3 \times 10^8\,\mathrm{s}^{-1}$. The continuous line shows $p_{\rm abs}(t)$ according to the optical Bloch equations (OBE). The long-dashed line shows the figure given by the rate equation (RE). The short-dashed line shows what absorption would correspond to an all-times matching of the excited population with the instantaneous laser illumination, in a quasi-static (QS) hypothesis. The dot-dashed line is the power $\overline{p}_{\rm abs} = \Gamma\,\overline{\rho}_{ee}$ dissipated from the excited state in the QS model, the time-integral of which is equal to the one of the total QS absorption power (short-dashed line). The double-dot-dashed line shows the instantaneous excitation rate $T_{g\leftrightarrow e}$, which the low-excitation (LE) hypothesis equates with the net absorption rate. The early peak and negative rebound of the QS-calculated absorption power are artefacts of the QS hypothesis, which forces the excited population to follow the laser pulse instantaneously, with artificially sharp population transfers; with the given parameters, the more rigorous OBE- and RE-calculated absorption rates remain positive at all times.

integral of all four absorption profiles can be expected to produce very similar results. The trend is confirmed at higher pressures, as normal. This is a strong incentive to focus experimental measurements on frequency-integrated values, and not just resonant absorption rates, especially with narrowband lasers.

2.8. Dependency of the overall attenuation on the absorption timing

When the experimentally measured quantity is the amount of light transmitted, after a given laser pulse has crossed an optically thick cell, the question arises whether the changes undergone by the laser time profile, due to the complicated timing of atomic absorption, can induce a significant dependence of the macroscopic laser pulse attenuation on the model used to describe this timing. Numerical modeling of the total absorption with the orders of magnitude given by table 2 shows a difference less than 0.1 % between the RE (4) and QS (16) models, even when the absorption length is

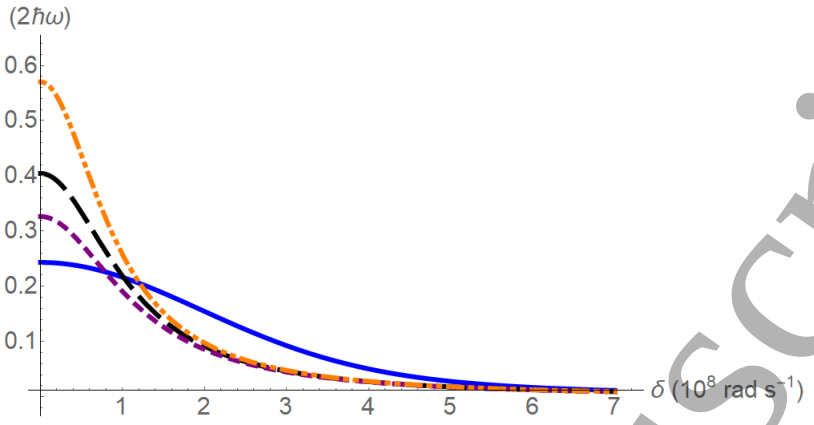

Figure 3. Time-integrated absorption by a xenon atom (in units of $2\,\hbar\omega$), for the same 1 mJ laser pulse as figure 2, as a function of the detuning δ with respect to the excitation energy of the $6p'[1/2]_0$ level, in units of 10^8 rad/s. The continuous line follows integration of the optical Bloch equations (OBE). The long-dashed line shows the figure given by the rate equation (RE). The short-dashed line is the output of the quasi-static model (QS). The double-dot-dashed line is the result of the low-excitation (LE) hypothesis. The ordinate at $\delta = 0$, for each model, is just the time integral of the curve presented on figure 2.

extended to 2 m. This gives us confidence that we can appropriately model absorption by a macroscopic sample, in our experiment, with the simpler model.

2.9. Two-photon absorption in a finite length cell in the quasi-static approximation and low-excitation limit

Modeling the attenuation of a pulsed, time-dependent laser with a flux $\Phi(x, y, z, t)$ that goes through a cell with a finite length z gets immensely simplified by assuming, as just suggested, that one can rely on the quasi-static (QS) model (as defined in subsection 2.5), i.e. an absorption rate that depends only on the total atomic density and the instantaneous laser intensity, for the calculation of overall absorption integrals. The hypothesis that most of the atomic population remains in the atomic ground state at all times is conditional to using the even simpler form of QS absorption, namely the low-excitation (LE) limit, given by equation (16). The latter criterion is not strictly fulfilled for the highest pulse energy (1 mJ) and lowest xenon pressure (1000 Pa) used in the experiment, for the OBE predict, in that case, that the population of the excited state goes up to ca. 12% at resonance. However, numerical simulations also show in this case that overestimation of the absorption by the QS+LE approximation gets mitigated by integration of the observed response on the frequency scale, on the whole width of the absorption profile (see subsection 2.7).

Under these conditions, assuming that the laser propagates along the z-axis with a unique velocity c, i.e. with no group-velocity dispersion, one can describe the attenuation of the light flux Φ in every propagating slice of the pulse by equation

$$\frac{\partial \Phi}{\partial z} = -2n\sigma^{(2)}\Phi^2 \tag{17}$$

Straightforward integration of (17) provides the formula that shows, at every time t, what flux $\Phi(z)$ is left from a flux $\Phi(0)$ that entered the cell at time $t - z/c$:

$$\Phi(z) = \frac{\Phi(0)}{1 + 2n\sigma^{(2)}\Phi(0)z} \tag{18}$$

The few ns' delay between the entry and exit points of the absorption cell is of course not a problem for the subsequent time integration that will give the transmitted energy of the laser pulse. Formula (18) is valid even for optically thick samples, leading to high attenuation factors, which is not incompatible with the hypothesis that every absorbing atom, individually, remains only weakly excited.

2.10. Two-photon absorption of a spatially Gaussian beam

Attenuation, however, is usually measured as the attenuation of the whole laser beam, which has a finite diameter and a transversely non-uniform intensity. Assuming that the beam has a Gaussian profile may not be unrealistic, and presents the advantage of making analytic integration possible. In this case, the flux profile can be written

$$\Phi(x, y, 0) = \Phi_0 \, \mathrm{e}^{-2\left(\frac{x^2}{w_x^2} + \frac{y^2}{w_y^2}\right)} \tag{19}$$

with w_x and w_y the waist parameters of the beam. For the sake of compactness, a symmetric form $\exp(-2r^2/w^2)$ will be used subsequently (generalization to the asymmetric case is straightforward). When dealing with samples the thickness of which z remains smaller than the Rayleigh length $Z_R = \pi w^2/\lambda$ (typically several metres), one can assume that diffraction does not appreciably redistribute the intensities transversely. At every radius r inside the beam, attenuation then just follows the law given by equation (18)

$$\Phi(r, z) = \frac{\Phi_0 \, \mathrm{e}^{-2r^2/w^2}}{1 + 2n\sigma^{(2)}\Phi_0 \, \mathrm{e}^{-2r^2/w^2} z} \tag{20}$$

A compact expression of the attenuated photon flux $P(z) = \int_0^\infty \Phi(r, z) 2\pi r dr$ follows

$$P(z) = \frac{\pi w^2}{4n\sigma^{(2)} z} \ln\left(1 + 2n\sigma^{(2)}\Phi_0 z\right) \tag{21}$$

which can be developed in powers of the peak flux Φ_0 as

$$P(z) = \frac{\pi w^2}{2}\Phi_0 \left[1 - n\sigma^{(2)}\Phi_0 z + \frac{4}{3}\left(n\sigma^{(2)}\Phi_0 z\right)^2 + O\left(\Phi_0^3\right)\right] \tag{22}$$

meaning that the relative attenuation of the total power $\Delta_\mathrm{P} = \left(P(z) - P(0)\right)/P(0)$ is just

$$\Delta_{\mathrm{P}} = -n\sigma^{(2)}\Phi_0 z + \frac{4}{3}\left(n\sigma^{(2)}z\right)^2\Phi_0^2 + O\left(\Phi_0^3\right) \tag{23}$$

The formula shows, when compared to formula (18), that the first-order relative total power attenuation of the beam is only half of what it would be if all the light was transported at the peak power. As the absorption process is a non-linear one, the wings of the intensity distribution get substantially less attenuated than the beam central rays.

2.11. Two-photon absorption, taking the pulse time-profile into account

Meanwhile, the temporal profile of a laser pulse is never a square one. Assuming that the time-dependence of the laser intensity can be modeled by a time-varying factor $S(t)$, such that $S(t)$ is maximum at 1, one gets from (21) a general expression of the number of transmitted photons $N(z) = \int P(z,t)\,dt$ of the form

$$N(z) = \frac{\pi w^2}{4n\sigma^{(2)}z}\int_{-\infty}^{\infty}\ln\left(1+2n\sigma^{(2)}\Phi_0 S(t)z\right)\,dt \tag{24}$$

2.11.1. First order attenuation. Only few time profiles $S(t)$ do make it possible to write the integral in an analytical way. For low enough intensities, one can develop the integrand of (24) as in formula (22), in powers of Φ_0:

$$N(z) = \frac{\pi w^2}{2}\Phi_0\left[\int_{-\infty}^{\infty}S(t)dt - n\sigma^{(2)}\Phi_0 z\int_{-\infty}^{\infty}S(t)^2dt + O(\Phi_0^2)\right] \tag{25}$$

Attenuation is thus reduced, with respect to the $-2n\sigma^{(2)}\Phi_0 z$ relative attenuation of a beam with photon flux Φ_0, by a factor $\frac{1}{2}I_2/I_1$, with I_p the time integral $\int_{-\infty}^{\infty}S^p(t)dt$. The factor 1/2 is the one produced by the spatial Gaussian profile. Since $S(t)$ is maximum at 1, the I_2/I_1 ratio always produces a further reduction of the attenuation leading term. For a Gaussian time profile, this is a supplementary $1/\sqrt{2} \simeq 0.707$ factor. Any symmetric hyperbolic secant profile produces a reduction factor $2/\pi \simeq 0.637$. Asymmetric profiles of the form $t^n\exp(-t/\tau)$ have integral ratios $3\,e^2/32 \simeq 0.693$, $5\,e^3/144 \simeq 0.697$ and $105\,e^4/8192 \simeq 0.700$ for $n = 2$, 3 and 4, respectively, whereas profiles of the form $t^n\exp(-t^2/\tau^2)$ have integral ratios $3\,e/(8\sqrt{2}) \simeq 0.721$, $5\,e^{3/2}\sqrt{\pi/3}/32 \simeq 0.717$ and $35\,e^2/(256\sqrt{2}) \simeq 0.714$ for $n = 2$, 3 and 4, respectively. In summary, even though an infinite variety of analytic forms can be used to represent a laser pulse time profile, realistic ones always lead to I_2/I_1 ratios similar, within a few percent, to the $1/\sqrt{2} \simeq 0.707$ ratio of a Gaussian profile.

The peak flux Φ_0, however, is not the parameter readily accessible to experiments : Φ_0 must be expressed as a function of the total incident number N of photons

$$N_0 \equiv N(0) = \frac{\pi w^2}{2}\,\Phi_0 I_1 \tag{26}$$

leading, from (25), to a relative transmission coefficient

$$K(z) = N(z)/N_0 = 1 - 2\,\frac{n\sigma^{(2)}z}{\pi w^2}\,\frac{I_2}{I_1^2}N_0 + O(N_0^2) \tag{27}$$

Accordingly, the generalized cross-section $\sigma^{(2)}(\omega)$ can be obtained, for low absorption, measuring the input and output absolute photon numbers or pulse energies, through formula:

$$\sigma^{(2)}(\omega) = \frac{\pi}{2}\frac{w^2}{nz}\,\frac{I_1^2}{I_2}\,\frac{N_0 - N(z)}{N_0^2} \tag{28}$$

2.11.2. All order attenuation. Formula (27), however, is only a first-order approximation, for $N(z)$ cannot go on decreasing in a linear way, down to zero at a finite distance! An all-order compact expression of the transmitted number of photons can be obtained, with the laser pulse time profile taken into account, if one assumes that this time profile can be represented by a Gaussian function $S(t) = e^{-t^2/\tau^2}$. Having a time profile that extends to infinity in the past does not sound very realistic, but the rapid decrease of the intensity at |times| large with respect to the duration of the pulse makes it a minor difficulty. The Gaussian profile can thus be considered as a realistic distribution of the pulse energy among large, small and intermediate intensities. In this model, the integral of formula (24) takes the form $2\times\int_0^\infty \ln\left[1 + a\exp(-t^2/\tau^2)\right]\,dt$, with $a = 2n\sigma^{(2)}\Phi_0 z$. Substituting variable t with $u = \exp(t^2/\tau^2)$, then making an integration by parts, one finds the latter integral equal to $\tau\int_1^\infty a\ln^{1/2}(u)/[u(u+a)]du$, which is the form of the most common integral-form definition of the polylogarithmic function of order 3/2, $\mathrm{Li}_{3/2}(-a)$. Finally

$$K(z) = \frac{\mathrm{Li}_{3/2}\left(-2n\sigma^{(2)}\Phi_0 z\right)}{-2n\sigma^{(2)}\Phi_0 z} \tag{29}$$

Expansion of $K(z)$ as a series of powers of $-2n\sigma^{(2)}\Phi_0 z$ has already been published by Rumi & Perry (2010), whose formula (41) gives the same result as (29). As a limitation noted by these authors, however, the sum of the series converges only if $2n\sigma^{(2)}\Phi_0 z < 1$. The polylogarithmic function, in contradistinction, has the advantage of not being restricted to a finite convergence radius. Formula (29) applies even to strong absorption regimes.

Since the time integral can be split in a sum of two separate integrals, one from $-\infty$ to 0 then another from 0 to ∞, the same formula still holds for any asymmetric time profile with Gaussian rise and fall, namely an e^{-t^2/τ_1^2} rise at negative times t followed by an e^{-t^2/τ_2^2} decrease at positive times t, usually with $\tau_2 > \tau_1$. The only complication is a more general definition of the time constant: $\tau = (\tau_1 + \tau_2)/2$. This actually makes the model suitable for a large variety of pulse shapes and durations.

Equation (29) makes it conspicuous that the transmission essentially depends on the peak power of the incident laser pulse. The pulse characteristic duration becomes an important parameter, however, if the experiment does not directly provide the peak instantaneous power, but the integrated energy or number of photons N_0 of the pulse:

$$K(z) = -\frac{\pi^{3/2}}{4}\frac{w^2\tau}{n\sigma^{(2)}N_0\,z}\,\mathrm{Li}_{3/2}\left(-\frac{4}{\pi^{3/2}}\frac{n\sigma^{(2)}N_0}{w^2\tau}z\right) \tag{30}$$

This includes a first-order attenuation of the form

$$K(z) = 1 - \frac{\sqrt{2}}{\pi^{3/2}}\frac{n\sigma^{(2)}N_0}{w^2\tau}z + O(N_0^2) \tag{31}$$

This is just the same as (27) in the special case of a Gaussian time-profile, where $I_2/I_1 = 1/\sqrt{2}$, and the same, at first order, as formula (20) of Di Rosa & Farrow (1999) for the case of zero photoionization. The $1/N(z) - 1/N_0 \propto z$ formula of Di Rosa & Farrow (1999) however leads to a more rapid decrease, at higher orders, than formula (29). This is a consequence of their assuming that the beam keeps a Gaussian profile, even though its more intense core undergoes a greater attenuation than its less intense, outer parts. This implies transferring a fraction of the beam intensity from its lesser to its more intense parts, hence making the attenuation artificially greater.

2.12. Expected transmission ratio

An example, for the expected transmission coefficient at the resonance frequency, can be calculated using formula (29) or (30), with the parameters given by table 2. Assuming that the Doppler effect dominates all other causes of spectral broadening, one obtains $K(z) \simeq 68\%$, i.e., by subtraction, a 32% absorption rate. This is very significantly different from the lowest-order approximation given by (31), which would yield a 58% absorption. Formula (20) of Di Rosa & Farrow (1999) yields a slightly better approximation, with a 37% absorption rate.

Formula (29) also shows that, as regards parameters that can be varied experimentally, the transmission coefficient expected at resonance $K(z)$ depends on the cross-section and photon flux only through the $n\Phi_0$ product, which, in the example, was $1.73 \times 10^{53}\,\mathrm{m^{-5}s^{-1}}$. With the assumed cross-section and cell length, the values 1, 3, and $5 \times 10^{53}\,\mathrm{m^{-5}s^{-1}}$ of the $n\Phi_0$ product lead to $K(z) \simeq 77$, 57 and 47%, respectively.

2.13. From the absorption profile to the cross-section

Assuming a Gaussian laser profile both in space and time, one can invert formula (30) numerically to translate every recorded transmission into an experimental value of the dimensionless argument $4\pi^{-3/2}\,n\,N_0\,z\,\sigma^{(2)}(\omega)/\left(w^2\tau\right)$. Obtaining a pure $\sigma^{(2)}(\omega)$ distribution is then just a matter of giving the cross-section its appropriate dimension, using the measured gas density n, total number of photons in the pulse N_0, laser beam waists w_x and w_y, and characteristic pulse duration τ.

As different experimental conditions can lead to spectral broadening with variable widths, the maximum absorption reached experimentally usually reflects but undirectly the atomic transition properties. But, provided that the observed transmission $K(\omega)$ can be reduced to give a complete $\sigma^{(2)}(\omega)$ function, integration via formula (8) yields

$\bar{\sigma}^{(2)}$ anyway. Application to the present experiment is described in section 4.1, with determination of the total cross-section illustrated by figure 5.

2.14. Other phenomena

2.14.1. Inhomogeneous broadening. In practice, absorption by the xenon vapor cumulates absorption by Xe atoms of all velocities, the absorption resonances of which are Doppler-shifted, with respect to the atomic frequency ω_0, according to the Gaussian distribution

$$D(\omega-\omega_0)=\frac{c}{2\omega_0}\sqrt{\frac{M}{2\pi k_B T}}\times e^{-\frac{1}{2}\frac{Mc^2}{k_B T}\frac{(\omega-\omega_0)^2}{\omega_0^2}} \tag{32}$$

where M and T stand for the atom mass and the absolute temperature, respectively, assuming, as for previous quantities, that D has been normalized on a 2ω scale. A Doppler-distributed cross-section $\sigma_{\mathrm{D}}^{(2)}(\omega)$ can thus be written as

$$\sigma_{\mathrm{D}}^{(2)}(\omega)=\int \bar{\sigma}^{(2)}\ g(\omega-\omega')\ D(\omega'-\omega_0)\ 2d\omega' \tag{33}$$

As long as the homogeneous resonance profile g does not get significantly broadened by collisions, i.e. at sufficiently low pressures, and in the absence of a hyperfine structure, the Doppler distribution D, at room temperature, is orders of magnitude broader than g, which makes the convolution of the two normalized distributions practically identical to $D(\omega-\omega_0)$. One may thus be tempted to substitute the Doppler distribution D for g, in the expression of $\sigma^{(2)}(\omega)$. One should remember, however, that the effective frequency-dependent cross-section $\sigma_{\mathrm{D}}^{(2)}(\omega)\simeq\bar{\sigma}^{(2)}D(\omega-\omega_0)$ only stands as an average cross-section of the Xe gas, which includes both a minority of resonant atoms and a majority of atoms shifted out of resonance by Doppler effect. As a consequence, this effective cross-section cannot be used to gauge the excitation regime of the few optically active atoms, the dynamics of which remains to be analyzed using the earlier described two-level models. Comparison of their outputs, in subsection 2.7, showed that the orders of magnitude, in the present experiment, are such that even at the lowest vapor density and highest pulse energy used, integration of the obtained cross-section over the whole width of the resonance line still provides a reliable value of the total cross-section $\bar{\sigma}^{(2)}$. As long as the laser intensity remains low enough not to make the system enter a fully saturated regime, this sum rule remains valid whatever the relative widths of the homogeneous and inhomogeneous line widths. This is only one more incentive for measuring the cross-section on the whole width of the resonance line then integrating it, rather than measuring the absorption at resonance only, since that latter method would make the subsequent determination of $\bar{\sigma}^{(2)}$ dependent on a complex model of the resonance profile.

2.14.2. Additional absorption due to photoionization. At the energy reached after two-photon absorption, about $9\times10^6\,\mathrm{m}^{-1}$ or more than 11 eV, the ionization threshold of

Xe, 12.13 eV, can easily be passed by absorption of a third photon, starting from the bound excited level. This additional absorption term must, in principle, be taken into account when assessing the observed laser beam attenuation.

The photoionization cross-section has been estimated by Chang & Kim (1982) for several Xe configurations, including the $5p^5 6p$ one and confirmed experimentally (Kröll & Bischel 1990). The expected value, for the absorption of a third photon following 2-photon absorption either at 222.6 or 224.3 nm, is about $1.5 \times 10^{-24}\,\mathrm{m}^2$. Even with a peak flux of $1.3 \times 10^{29}\,\mathrm{s}^{-1}\mathrm{m}^{-2}$, for a duration of 6 ns, this is only little more than a 0.1% photoionization probability. Given the facts that i) all atoms are not submitted to the peak flux ii) population of the bound excited level does not grow instantaneously, photoionization, within the precision of the present study, can be considered negligible.

2.14.3. Amplified spontaneous emission. The possibility of having TALIF measurements perturbed by amplified spontaneous emission (ASE), which would depopulate excited levels much more rapidly than ordinary spontaneous emission, was signaled in the 1980s (Aldén et al. 1989). ASE was observed following two-photon excitation of O atoms, for lower densities than the Xe densities of the present study, but with a focused laser (Amorim et al. 1994). Stimulated emission was also observed specifically from the $6p'[1/2]_0$ and $6p'[3/2]_2$ levels of xenon, following excitation with "mildly focused" 15 ns pulses with an energy 0.1 to 0.5 mJ (Alekseev et al. 2017). ASE, anyway, is not as big a problem, for absorption-based measurements, as it has been for fluorescence measurements. By bringing the excited atomic population faster back to the ground level, ASE, in fact, would only make the low-excitation hypothesis a better approximation.

2.14.4. Nontrivial photon statistics. In the case of polychromatic or multimode laser light, evolution of the atomic system compounds all spectral components of the exciting light. Moreover, even when the spectral width of the excitation laser remains small with respect to β, the appropriate square photon flux Φ^2 to be put in equation (6) is not just proportional to the square of the short-term time-averaged light intensity $\bar{I}(t)$ that can be measured with laboratory power-meters, even with a sub-ns time resolution. As for the efficiency of non-resonant (hence quasi-instantaneous) coherent two-photon absorption, $\bar{I}(t)^2$ must be multiplied by the second-order coherence factor of the field, $G^{(2)}(0)$, and the effective flux Φ to be put into equation (6) is such as

$$\Phi(t)^2 = G^{(2)}(0) \left(\frac{\bar{I}(t)}{\hbar\omega} \right)^2 \tag{34}$$

Measurements that rely on linear measurements of finite-time resolution intensity $\bar{I}(t)$, with no characterization of the second-order coherence factor, will thus only reveal an effective cross-section

$$\hat{\sigma}^{(2)}(\omega) = G^{(2)}(0)\, \sigma^{(2)}(\omega) \tag{35}$$

Multimode chaotic light, with $G^{(2)}(0) = 2$, can lead in this way to an apparent cross-section $\hat{\sigma}^{(2)}$ twice higher than $\sigma^{(2)}$. This is the reason why the present work has used a single-mode laser, with $G^{(2)}(0) = 1$, to measure the two-photon cross-section in an unambiguous way. An advantage of simultaneous Xe calibration, for TALIF-based oxygen density measurements, is that using the same laser for both O and Xe measurements, one does not need to know the $G^{(2)}(0)$ factor: the relevant $\hat{\sigma}_{\mathrm{Xe}}/\hat{\sigma}_O$ ratio is the same as the $\sigma_{\mathrm{Xe}}/\sigma_O$ ratio.

2.14.5. Hyperfine splitting. By convention a number of integrated cross-sections available in the literature, including the 2-photon excitation cross-section of the $6p'[3/2]_2$ level of Xe I, have even included a sum on unresolved hyperfine and even fine structure components. In such cases, an individual cross-section and transition rate can be associated to every component, which makes the Ω value given by an unresolved application of formula (11) an upper limit of these underlying nutation frequencies.

3. Experimental set-up

3.1. Gas cell

As depicted by figure 4, the experiment takes place in a cylindrical, 0.51 m long gas cell equipped with windows set at Brewster's angle. The cell is filled with Xe gas at a pressure between 100 and 10^4 Pa, the static value of which is monitored with a Thermovac TM 101 (Oerlikon Leybold Vacuum) pressure gauge. These pressure measurements are checked by a posteriori calibration with a more precise, capacitive, CMR 362 (Pfeiffer vacuum) pressure gauge. The obtained precision is about 1% (resp. 5%) for pressures above (resp. below) 1000 Pa. The assumed temperature, for atomic density calculations, is 23°C, i.e. 296.15 K. Daily temperature variations of the order of ±2°C have added an additional uncertainty of ±0.7% on the density.

3.2. Laser beam and energy measurements

The spatial shape of the laser beam has been monitored, both before and after the cell, with a BC106N-UV - CCD camera beam profiler (Thorlabs). Relative variations of either the w_x or w_y waist parameter, before and after the cell, remain within a ±10% interval. An average of the input and output waists, in both directions, has been used for numerical simulations.

The transmitted energy and a fraction of the incident one (about 2% of the incoming beam, as transmitted by the last, nearly totally reflecting mirror) are simultaneously recorded, on a shot-by-shot basis, via a two-channel Pulsar-2 (Ophir) interface. The transmitted laser pulse energy is measured with an Ophir PE10-C pyroelectric energy meter, the precision of which is supposed to be ±8% downto 240 nm. According to the manufacturer, the precision can be estimated using the spectral response of the metallic absorber of the detector, which gives a ±10% uncertainty at 230 nm. However,

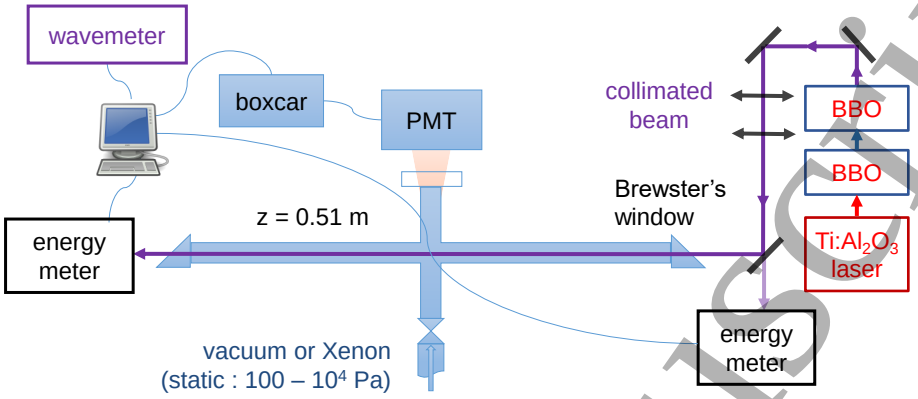

Figure 4. Experimental setup with the gas cell equipped with Brewster's angle windows, the Ti:sapphire laser system with the β-barium-borate (BBO) frequency doublers used to bring the output radiation into the 220 nm range, energy meters, the photomultiplier tube (PMT) used to collect the fluorescence radiation and the data acquisition network.

checks carried out with a QE 12 LP-S-MB-D0 (Gentec) detector, also with a given precision of $\pm 10\%$, have provided values systematically greater by a factor 1.27. As a compromise, we have retained the former measurements, with a 1.15 correction factor and an uncertainty $\pm 10\%$.

Absolute measurement of the laser pulse energy is carried out only at the exit of the cell, with a 1/0.99 corrective factor introduced as a correction for the 1% loss ratio measured when going through the output window. Scanning the laser throughout the absorption resonance makes the input energy accessible, below and above resonance, where absorption reduces to zero. Interpolation then provides us with the trend of the input energy across the resonance, as shown by figure 5 a). The input energy gets indirectly measured, throughout resonance, on a shot-to-shot basis, using the variation of the 2% fraction of the beam extracted just before the absorption cell to rescale the absolute energy reference.

Furthermore, as shown by figure 6, the profiler reveals that up to 20% of the input power can be transported in a peripheral low-intensity structure, outside the central Gaussian profile of the beam. This ratio is measured everyday and the corresponding energy is subtracted from both the input and output, to give the relevant $N_0\hbar\omega$ quantity that must be taken into account as the input through the main, axial structure. As regards the peripheral structure, because of its comparatively larger area and lower intensity, it undergoes two-photon absorption only in a negligible way, which is the reason why the same absolute energy has to be subtracted from the measured and estimated, transmitted and input energy, respectively.

Fluorescence, although not essential in our measurement scheme, is monitored with

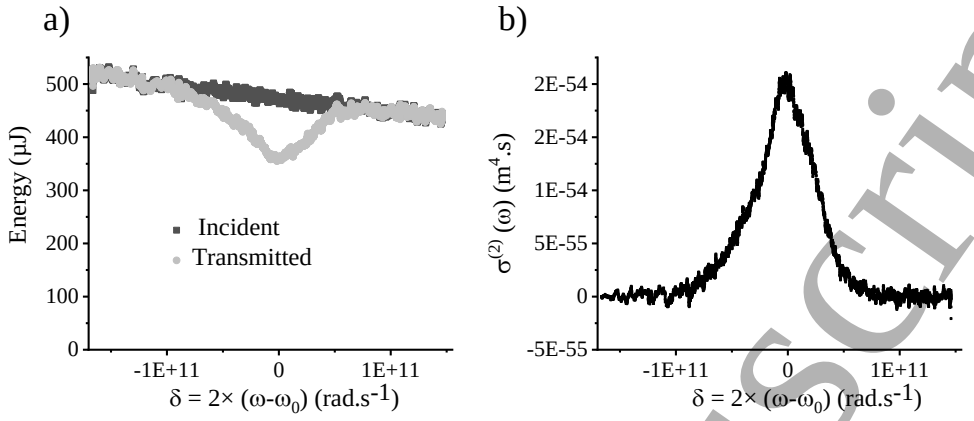

Figure 5. Absorption profile of the $6p'[3/2]_2$ resonance, for a density of 1.63×10^{24} atoms/m^3, with waist parameters w_x and w_y of 323 and 305 μm respectively and a measured characteristic pulse duration of 6.4 ns. Every point is a 20-shot average. a) The transmitted energy (light grey) is compared to the input (dark grey), with a linear normalization of the latter assuming that the two are equal on both sides of the atomic resonance. b) Starting from the transmission coefficient $K(\omega)$ obtained as the output/input ratio, inversion of formula (30) provides the $\sigma^{(2)}(\omega)$ resonance profile. A peak value of about 2×10^{-54} m^4 s^{-1} and a full width at half maximum of the order of 0.7×10^{11} rad s^{-1} immediately give an integrated cross-section about 1.4×10^{-43} m^2.

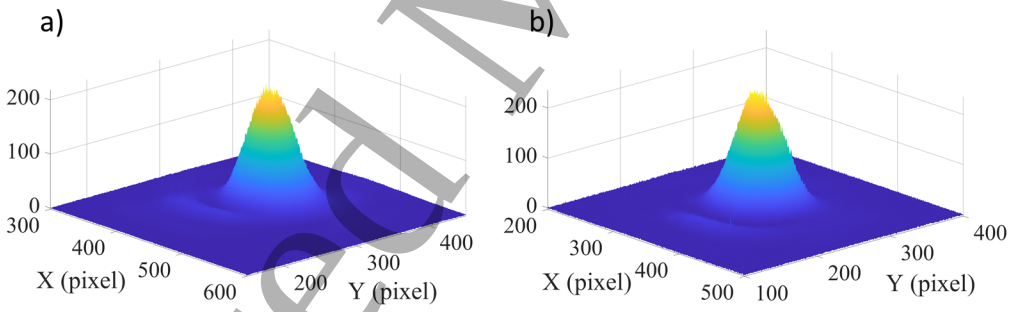

Figure 6. Two-dimensional relative intensity profile of the laser beam (arbitrary units), before (a) and after (b) the absorption cell. Despite its very low relative intensity, the secondary structure that appears in both profiles at larger radii, outside the central Gaussian peak, can contain as much as 20% of the total flux. The pixel size is $6.45 \times 6.45\,\mu$m^2.

a R3896 (Hamamatsu) photo-multiplier, through an interference filter centered at the wavelength 840 nm, with a 13 nm full width at half-maximum.

3.3. Temporal characteristics

The time profile of the laser pulse has been monitored with an ET-2030A (Electro-Optics Technology) photodiode and a *Wavepro* 725Zi (LeCroy) 2.5 GHz oscilloscope. Numerical modeling shows that, for a typical pulse duration $\tau \simeq 6.4$ ns, the combined risetime $\simeq 0.45$ ns of the diode and scope increases the characteristic pulse duration

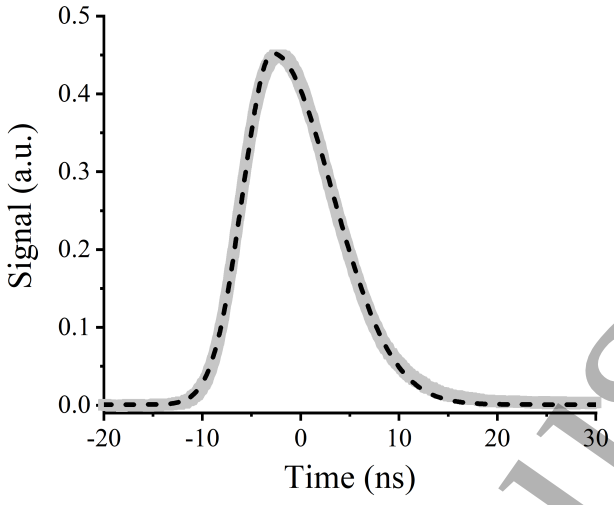

Figure 7. Measured time profile of the laser pulse (grey), and how it can be fitted by an asymmetric Gaussian profile (dashed line) with characteristic rise and fall times of 4.27 and 8.59 ns, respectively, hence an average 6.43 ns characteristic duration. Injection seeding by a continuous-wave laser makes the laser pulse build up on a single cavity mode, which results in a smooth profile, free of any longitudinal mode beating. Excellent correspondence between the data and the fitting formula guarantees that the error due to analytical modeling of the time profile remains lower than 1%.

by only 0.02 to 0.03 ns. This slight increase, even though a very small one, has been subtracted from the raw duration measurements to feed the analysis of the data with unbiased laser pulse durations. Care must be taken to sample the laser beam exactly on axis, for the light pulse can appear significantly shorter in the outer parts of the laser beam. Figure 7 shows how well the asymmetric-Gaussian fits the recorded time-profile.

3.4. Spectral characteristics

The pulsed laser used is a single-mode injection-seeded Ti:Sa laser that was developed in the laboratory for spectroscopic studies and described in details previously (Lottigier et al. 2019). The laser bandwidth, at the fundamental wavelengths 890.3 and 897.2 nm, is less than 30 MHz. The laser is sent through two successive β-barium borate (BBO) frequency-doubling crystals, in order to produce the necessary radiation, at the wavelength 222.6 or 224.3 nm, before entering the gas cell.

4. Results

4.1. Linearization of the absorption profile and integrated cross-section

The laser time profile is measured several times everyday, at the beginning of every new scan of the absorption profile. As already explained in subsection 2.13, absolute measurement of the output and input photon numbers and the laser wavenumber for

every pulse provides us with a sample of the transmission function $K(\omega)$, which can be linearized into an experimental $\sigma^{(2)}(\omega)$ distribution by inversion of formula (30). An example of such a linearized $\sigma^{(2)}(\omega)$ profile is given by figure 5 b). Integration over 2ω, according to formula (8), then provides an experimental value of $\bar{\sigma}^{(2)}$. The whole set of obtained $\bar{\sigma}^{(2)}$ values is given by figure 8, for different values of the $n \times \Phi_0$ product (which acts as a multiplier of the cross-section inside the dimensionless argument of the transmission function, as shown by formula (29) explicitly).

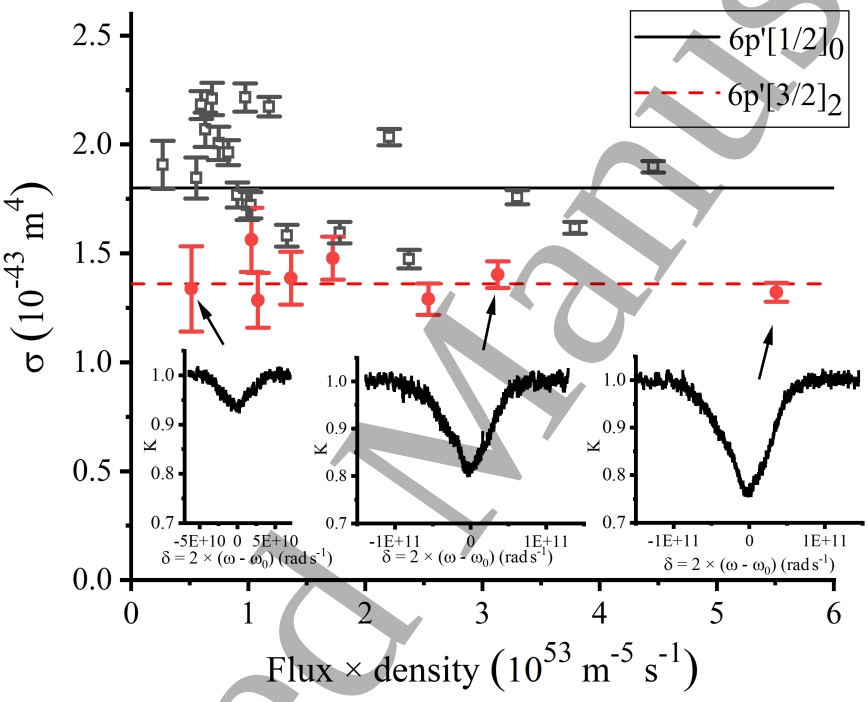

Figure 8. Measured cross-sections, for the $6p'[3/2]_2$ and $6p'[1/2]_0$ levels and different values of the $n \times \Phi_0$ factor, the product of which with $\bar{\sigma}^{(2)}$ determines a weaker or stronger absorption regime. Insets show three corresponding examples of experimental transmission profiles, which make it visible that the stronger the absorption, the better the relative precision on it. For these three examples at, roughly, $n\Phi_0 = 0.5$, 3.2 and $5.5 \times 10^{53}\,\mathrm{m}^{-5}\mathrm{s}^{-1}$, the minimum transmission K, according to formula (29), would be 89%, 62% and 51% respectively. The slightly higher minimum transmission observed results from additional broadening by the underlying hyperfine structure of the odd isotopes and pressure broadening. The uncertainty bars drawn around the determined cross-sections only reflect the numerical uncertainty that comes out with integration of the $\sigma^{(2)}(\omega)$ resonance profile. A total uncertainty bar would also include uncertainty on the laser waist parameters, pulse energy and time profile, all of which also exhibit variations. Apart from these fluctuations, both measured cross-sections appear, as required, fairly independent on the weaker or stronger absorption regime.

According to our measurements, the generalized cross-section $\overline{\sigma}^{(2)}$ appears to be $1.36^{+0.46}_{-0.34}$ and $1.88^{+0.75}_{-0.54} \times 10^{-43}\,\mathrm{m}^4$ for the $6p'[3/2]_2$ and $6p'[1/2]_0$ levels, respectively. The former appears more than a factor of 2 (albeit the exact factor cannot be told but with a

more than ±50% uncertainty) smaller than what had been deduced from the measured Xe/O cross-section ratio (Niemi et al. 2005) and the measured 2-photon cross-section of oxygen at 226 nm (Bamford et al. 1987): $\overline{\sigma}^{(2)}(6p'[3/2]_2) = 1.9(2) \times 1.87(60) \times 10^{-43} = 3.6^{+1.7}_{-1.4} \times 10^{-43}\,\mathrm{m}^4$.

Table 3. Origin of the uncertainty

Parameter	Relative uncertainty
Statistical dispersion	±7%/ ± 12%
Laser pulse energy	±13%
Laser waist parameters	±6%
Pulse characteristic duration	±1%
Cell length	±1%
Temperature	±1%
Pressure	±1%

The uncertainty budget is given by table 3. The ±7% vs. ±12% figure of statistical dispersion corresponds to the $6p'[3/2]_2$ and $6p'[1/2]_0$ final levels, respectively. The resulting relative uncertainty on the measured cross-sections, calculated as the product of all uncertainty factors, is 1.00^{+34}_{-26} or 1.00^{+40}_{-29}, respectively.

4.2. Cross-section ratios and the available theoretical data on excitation channels

4.2.1. A $J' = 0/J' = 2$ ratio found similar to the result of previous studies. Because a large fraction of the uncertainty comes from possible systematic errors that affect both measurements equally (especially the rather large possible bias on the laser pulse energy), the cross-section ratio can be estimated with a precision better than the absolute cross-sections. In the present experiment we get $\overline{\sigma}^{(2)}(6p'[1/2]_0)/\overline{\sigma}^{(2)}(6p'[3/2]_2) = 1.38^{+21}_{-18}$. This corroborates the 1.2 and 1.1 values (the latter with a factor 2-3 of uncertainty) found by Alekseev & Setser (1996) and Eichhorn et al. (2011), respectively.

4.2.2. A reason for the final $J' = 0$ preponderance found in Racah algebra. Since for the channels considered the excited electron always ends up in a $6p'$ state, one can imagine that a great part of the cross-section ratio comes from the angular algebra that makes either a $J' = 0$ or a $J' = 2$ from a ^2p electron coupled with a $j = 1/2$ atomic core. Assuming, more precisely, that the excited states of xenon we deal with are pure $|((5p^5)j, \ell)\,[K]_J\rangle$ eigenstates with a $(5p^5)j$ core left unperturbed by any transition between them (hence always in a $j = 1/2$ fine-structure excited state), we can develop the d_{eq} matrix elements of formulae (1) to (9), according to standard angular momentum algebra, into:

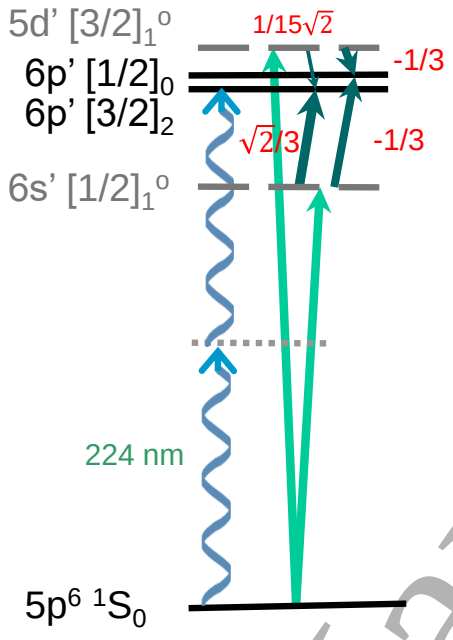

Figure 9. For each possible final level, the two-photon excitation (couple of wavy arrows) is fed by coherent superpositions of successive amplitudes (straightline arrows), which must go through intermediate states in a transient way. But while the $6p'[1/2]_0$ benefits evenly from amplitudes built through the $6s'[1/2]_1^o$ and $5d'[3/2]_1^o$ levels, the $6p'[3/2]_2$ final level gets essentially fed through the intermediate $6s'[1/2]_1^o$ only, due to a very unfavorable $\frac{1}{15\sqrt{2}}$ angular coefficient from the $d'[3/2]_1^o$ level. Moreover, the $6p'[1/2]_0$ excitation amplitude, exclusively, also contains a significant term via the $6d[3/2]_1^o$ intermediate level (not represented). .

$$d_{eq} = (-1)^{J+J'+K+K'+j+s+\ell'}[J,J',K,K']^{1/2}\begin{pmatrix} J' & 1 & J \\ 0 & 0 & 0 \end{pmatrix}\begin{Bmatrix} J & 1 & J' \\ K' & s & K \end{Bmatrix}\begin{Bmatrix} K & 1 & K' \\ \ell' & j & \ell \end{Bmatrix}\langle \ell' || D || \ell \rangle \tag{36}$$

with ℓ and s the orbital angular momentum and spin of the excited electron, respectively ($s = 1/2$), and D the appropriate component of the electric dipole operator. The primed and unprimed quantum numbers are those of the final state $|e\rangle$ and an intermediate state $|q\rangle$, respectively. Bracket $[K]$ stands for $2K + 1$. The bottom row of zeros in the 3-j coefficient takes into account the fact that no excitation to a final state with $J' = 0$ can take place in circular polarization, so the comparison between the two cross-sections makes sense for linear polarization only.

The dominant contributions are those going through intermediate levels closest to the energy reached after absorption of one photon. Each term of the total amplitude, in formulae (1) to (9), also depends on the involved radial matrix element $\langle \ell' || D || \ell \rangle$ and the other matrix element, $d_{qg} = \langle q|D|g\rangle$, between the ground and intermediate states. The order of magnitude of every path, however, depends in a decisive way on the value

of the angular coefficient given by formula (36). Would the transition amplitude to the $6p'$ states rely on dipole matrix elements with intermediate s'^o states only, the transition amplitude to the $6p'[3/2]_2$ level would be $\sqrt{2}$ larger, hence the cross-section twice larger than the $6p'[1/2]_0$ one. As shown by figure 9 however, reinforcement of the amplitude by a term with $|5d'[3/2]_1^o\rangle$ as the $|q\rangle$ state tilts the balance the other way, for it turns out that $|6p'[1/2]_0\rangle$ is the only one of the two final states that takes advantage from this reinforcement, while the angular coupling from the $d'[3/2]_1^o$ to the $6p'[3/2]_2$ level appears peculiarly small.†

4.2.3. Possible reinforcement of the $J' = 0$ cross-section via the $|d[3/2]_1^o\rangle$ states. Examination of contributing couples of dipole matrix elements (Aymar & Coulombe 1978, Salah & Hassouneh 2019), namely those leading to either the $6p'[1/2]_0$ or the $6p'[3/2]_2$ levels via $6s'$, $7s'$, $5d'$, $6d'$, $7d'$, and $6s$, $7s$, $5d$, $6d$, $7d$ $J = 1$ states, an excerpt of which is given by table 4, confirms that the $6s'[1/2]_1^o$ and $5d'[3/2]_1^o$ levels produce dominant contributions to the 2-photon excitation amplitudes. A very significant contribution, however, also comes from the "unprimed" $(5p^5)_{j=3/2}\,5d\,[3/2]_1^o$ and $6d\,[3/2]_1^o$ intermediate levels, specifically to the final $6p'[1/2]_0$ level. A significant feature, in the very case of the former calculation (Aymar & Coulombe 1978), may be that the intermediate $6d\,[3/2]_1^o$ and the final level are very close in energy.

Table 4. Energy detuning factor, dipole matrix elements (Aymar & Coulombe (1978)/Salah & Hassouneh (2019)) and resulting dominant two-photon amplitudes (absolute values, in atomic units), for those intermediate states $|q\rangle$ leading to the largest partial amplitudes

Intermediate level	$\omega/(\omega_q - \omega_g - \omega)$	$\lvert\langle g\lvert\lvert r\rvert\rvert q\rangle\rvert$	$\lvert\langle q\lvert\lvert r\rvert\rvert e\rangle\rvert$	2-photon amplitude
to excited level $\lvert e\rangle = \lvert 6p'[3/2]_2\rangle$				
$6s'[1/2]_1^o$	1.37	0.66/0.50	2.25/2.83	2.03/1.92
$7s'[1/2]_1^o$	0.87	0.19/0.11	2.60/0.49	0.42/0.05
$5d'[3/2]_1^o$	0.91	1.42/1.10	0.43/0.57	0.55/0.57
$5d\,[3/2]_1^o$	1.13	1.20/1.04	0.29/0.12	0.39/0.14
to excited level $\lvert e\rangle = \lvert 6p'[1/2]_0\rangle$				
$6s'[1/2]_1^o$	1.39	0.66/0.50	1.33/1.96	1.22/1.36
$5d'[3/2]_1^o$	0.92	1.42/1.10	2.66/4.73	3.50/4.80
$6d'[3/2]_1^o$	0.81	0.69/0.59	1.66/1.56	0.93/0.74
$5d\,[3/2]_1^o$	1.15	1.20/1.04	0.71/0.78	0.98/0.94
$6d\,[3/2]_1^o$	1.00	0.71/0.70	2.94/0.82	2.09/0.58

Numerically, the matrix element from $|q\rangle = |5d'[3/2]_1^o\rangle$ appears larger to the $J' = 0$

†Looking at formula (36) in details, one finds that this smallness is due to both 6-j coefficients, since $\begin{Bmatrix} 1 & 1 & 2 \\ 3/2 & 1/2 & 3/2 \end{Bmatrix}$ and $\begin{Bmatrix} 3/2 & 1 & 3/2 \\ 1 & 1/2 & 2 \end{Bmatrix}$ are both equal to a remarkably small $\frac{1}{2\sqrt{30}}$.

than to the $J' = 2$ level by a factor 6.4 or 8.4, depending on the calculation, which compares well with the simplified $5\sqrt{2} \simeq 7.1$ angular ratio. The $|q\rangle = |6s'[1/2]^o_1\rangle$ intermediate state yields, more intuitively, a matrix element larger with the $J' = 2$ than with the $J' = 0$ by a factor of 1.67 or 1.42, depending on the calculation, to be compared with a $\sqrt{2} \simeq 1.41$. For comparisons where intermediate states of different configurations come into play, however, angular factors cannot tell the whole story. As an illustration, comparison of the $6s'/5d'$ contribution ratios with the purely angular factors of figure 9 shows that the $6s'$ amplitudes must benefit from a relative reinforcement by about a factor of 3, due to radial effects.

Specific information on the signs of the amplitudes is unfortunately missing with the published line strengths, which makes it yet impossible to predict the way these channels interfere. Re-evaluating the transition matrix elements of Xe I *ab initio* is beyond the scope of the present study.

4.3. Pressure effects

Pressure broadening and pressure shift of the excitation line can be observed at higher pressures, as shown by figure 10. Two-photon spectroscopy of the $6p[1/2]_0$, $6p[3/2]_2$ and $6p[5/2]_2$ have shown the same effects, which can be used to estimate the interatomic potential (Gornik et al. 1981). As shown in the inset, the resonance line undergoes a linear shift, as a function of the gas pressure, with a proportionality coefficient $-2.8(2)\times10^{-4}\,\mathrm{m}^{-1}/\mathrm{Pa}$, or $-2.2(2)\times10^{-15}\,\mathrm{m}^3\mathrm{s}^{-1}$ if expressed as an angular rate shift per unit of density. This is only slightly smaller than the $-2.5(2) \times 10^{-15}\,\mathrm{m}^3\mathrm{s}^{-1}$ coefficient found for the $6p[1/2]_0$ two-photon resonance (Gornik et al. 1981).

As far as it can be measured despite a growing asymmetry, the line also undergoes pressure broadening, with an increase of its half-width of the order of $6.7(1.3) \times 10^{-15}\,\mathrm{m}^3\mathrm{s}^{-1}$. The shift-to-half-width ratio is thus about -0.32(9), which appears quite compatible with the -0.357 ratio predicted in the impact approximation (Schuller & Behmenburg 1974).

As expected, the broadening coefficient appears significantly larger than the bare collisional de-excitation coefficient $k_Q \simeq 4.2 \times 10^{-16}\,\mathrm{m}^3\,\mathrm{s}^{-1}$ introduced in subsection 2.7. This is a confirmation that inelastic collisions are only a minor factor of line broadening, when compared to elastic collisions.

5. Conclusion

Calibration of the two-photon excitation cross-section of the $6p'[3/2]_2$ and $6p'[1/2]_0$ levels of xenon has provided us with an opportunity to revisit the models currently used to describe two-photon laser induced fluorescence. As a matter of fact, even with pulse durations as large as a few nanoseconds and without focusing, application of pure rate equations may appear questionable. Time- and frequency-scale integration may reduce the discrepancy between the simple predictions made on the basis of a steady-state

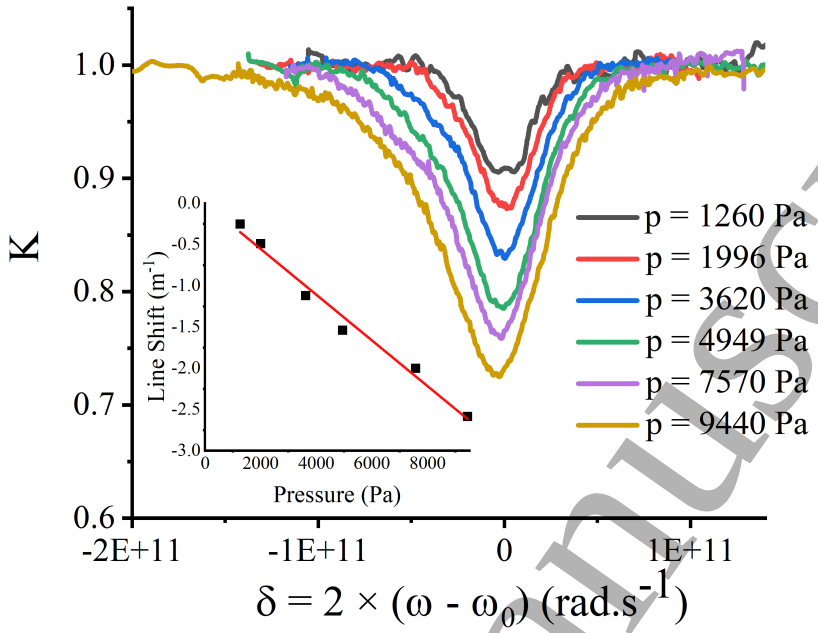

Figure 10. Variation of the absorption profile with pressure, in the vicinity of the $6p'[1/2]_0$ resonance. Inset: dependence of the $6p'[1/2]_0$ resonance position on Xe pressure.

excitation cross-section and the actually absorbed power. However, in cases where the laser power is such that saturation is reached, or for shorter pulses, quantitative analysis will always require a re-examination of the atom dynamics, at least in the coherent two-level atom model. Using absorption, rather than fluorescence observation, makes it possible to get rid of the uncertainties attached to the efficiency of fluorescence collection and de-excitation branching ratios. A new analytic formula has been proposed for the two-photon damping of resonant light in a long gas cell, which was successfully used to linearize transmission profiles, whatever the weaker or stronger absorption regime.

As a result, the measured $6p'[3/2]_2$ cross-section appears more than a factor of 2 smaller than what had been deduced from earlier measurements. The suspicion that some atomic O densities measured with Xe calibration may have been overestimated thus appears confirmed. Future TALIF measurements should take the reduced value of the Xe cross-section into account. Examination of the different intermediate states possibly involved in building the two-photon transition matrix element has explained, at least partly, why the 2-photon excitation cross-section of the $6p'[1/2]_0$ level could be larger than the $6p'[3/2]_2$ one, which can lead to recommend that the former, hyperfine structure-free, state be used instead. This counter-intuitive cross-section ratio may be due only to the accidentally low value of the angular coefficients that correspond to a $d'[3/2]_1$ to $p'[3/2]_2$ transition. Examining all different possible channels has also shown a larger-than-expected number of possibly non-negligible contributions, which shows how hazardous it may be to assume that a two-photon transition amplitude receives a

dominant contribution from one single intermediate state. Finally, the pressure shift of the $6p'[1/2]_0$ line was found similar to what has already been measured with several $6p$ states of xenon, whereas the shift-to-broadening ratio was found to agree with a standard model of collisional perturbation.

Similar investigations can be profitably considered with other states of xenon and other rare gas atoms also used for TALIF calibration.

Acknowledgments

The authors wish to thank J. Alkhoury, N. Romeo and T. Jannaud, for their participation in the experiments, together with J.-P. Booth, A. Chatterjee, O. Guaitella and A.S. Morillo-Candas, whose technical help was greatly appreciated. They also gratefully acknowledge stimulating comments by R.-J. Champeau, A. Crubellier, C. Delsart and J.-F. Wyart during the preparation of the manuscript.

References

Aanesland A, Liard L, Leray G, Jolly J & Chabert P 2007 *Appl. Phys. Lett.* **91**, 121502.
Abella I D 1962 *Phys. Rev. Lett.* **9**, 453.
Adams S F & Miller T A 1998 *Chem. Phys. Lett.* **295**, 305.
Aldén M, Edner H, Grafström P & Svanberg S 1982 *Opt. Commun.* **42**, 244.
Aldén M, Westblom U & Goldsmith J 1989 *Opt. Lett.* **14**, 305.
Alekseev V A, van der Burgt P J & Setser D 2017 *J. Chem. Phys.* **146**, 094304.
Alekseev V & Setser D 1996 *J. Phys. Chem.* **100**, 5766.
Allen L, Eagles K & Stroud Jr C 1982 *J. Phys. B: At. Mol. Phys.* **15**, 1643.
Allen L & Stroud Jr C R 1982 *Phys. Rep.* **91**, 1.
Amorim J, Baravian G, Touzeau M & Jolly J 1994 *J. App. Phys.* **76**, 1487.
Annušová A, Marinov D, Booth J P, Sirse N, da Silva M L, Lopez B & Guerra V 2018 *Plasma Sources Sci. Technol.* **27**, 045006.
Aymar M & Coulombe M 1978 *Atom. Data Nucl. Data* **21**, 537.
Bamford D J, Dyer M J & Bischel W K 1987 *Phys. Rev. A* **36**, 3497.
Bamford D J, Hickman A P, Dyer M J & Bischel W K 1988 *J. Opt. Soc. Am. B* **5**, 1369.
Bamford D J, Jusinski L E & Bischel W K 1986 *Phys. Rev. A* **34**, 185.
Bamford D J, Saxon R P, Jusinski L E, Buck J D & Bischel W K 1988 *Phys. Rev. A* **37**, 3259.
Bischel W K, Perry B E & Crosley D R 1981 *Chem. Phys. Lett.* **82**, 85.
Bischel W K, Perry B E & Crosley D R 1982 *Appl. Optics* **21**, 1419.
Blondel C, Alkhoury J, Jannaud T & Drag C 2020 *J. Phys.: Conf. Ser.* **1412**, 142012.
Bokor J, Freeman R R, White J C & Storz R H 1981 *Phys. Rev. A* **24**, 612.
Boogaarts M, Mazouffre S, Brinkman G, van der Heijden H, Vankan P, Van der Mullen J, Schram D & Döbele H 2002 *Rev. Sci. Instrum.* **73**, 73.
Brewer P, Das P, Ondrey G & Bersohn R 1983 *J. Chem. Phys.* **79**, 720.
Brewer P, Van Veen N & Bersohn R 1982 *Chem. Phys. Lett.* **91**, 126.
Bruce M, Layne W, Whitehead C & Keto J W 1990 *J. Chem. Phys.* **92**, 2917.
Cagnac B, Grynberg G & Biraben F 1973 *J. Phys. (Paris)* **34**, 845.
Chang T & Kim Y S 1982 *Phys. Rev. A* **26**, 2728.
Chen C, Hurst G & Payne M 1980 *Chem. Phys. Lett.* **75**, 473.
Dakka M, Tsiminis G, Glover R, Perrella C, Moffatt J, Spooner N, Sang R, Light P & Luiten A 2018 *Phys. Rev. Lett.* **121**, 093201.

Das P, Ondrey G, Van Veen N & Bersohn R 1983 *J. Chem. Phys.* **79**, 724.
Di Rosa M D & Farrow R L 1999 *J. Opt. Soc. Am. B* **16**, 1988.
DiMauro L, Gottscho R A & Miller T A 1984 *J. App. Phys.* **56**, 2007.
Dreyfus R, Jasinski J, Walkup R & Selwyn G 1985 *Pure Appl. Chem.* **57**, 1265.
Dyer M J & Crosley D R 1989 *Opt. Lett.* **14**, 12.
Eagles K, Stroud Jr C & Allen L 1982 *J. Phys. B: At. Mol. Phys.* **15**, 2021.
Eichhorn C, Fasoulas S, Auweter-Kurtz M, Loehle S & Leiter H 2011 *in* '42nd AIAA Plasmadynamics and Lasers Conference in conjunction with the 18th International Conference on MHD Energy Conversion (ICMHD)' p. 3460.
Elliott D, Scime E & Short Z 2016 *Rev. Sci. Instrum.* **87**, 11E504.
Fleurbaey H, Galtier S, Thomas S, Bonnaud M, Julien L, Biraben F, Nez F, Abgrall M & Guéna J 2018 *Phys. Rev. Lett.* **120**, 183001.
Goehlich A, Kawetzki T & Döbele H 1998 *J. Chem. Phys.* **108**, 9362.
Goldsmith J E 1987 *Appl. Optics* **26**, 3566.
Gornik W, Kindt S, Matthias E & Schmidt D 1981 *J. Chem. Phys.* **75**, 68.
Grischkowsky D, Loy M & Liao P 1975 *Phys. Rev. A* **12**, 2514.
Grynberg G & Cagnac B 1977 *Rep. Prog. Phys.* **40**, 791.
Heaven M, Miller T A, Freeman R R, White J & Bokor J 1982 *Chem. Phys. Lett.* **86**, 458.
Herring G, Dyer M J, Jusinski L E & Bischel W K 1988 *Opt. Lett.* **13**, 360.
Jiang C & Carter C 2014 *Plasma Sources Sci. Technol.* **23**, 065006.
Khambatta N M, Oertel J A, Silk R, Radziemski L J & Mack J M 1988 *J. App. Phys.* **64**, 4809.
Klochko A, Lemainque J, Booth J P & Starikovskaia S 2015 *Plasma Sources Sci. Technol.* **24**, 025010.
Kramida A, Yu. Ralchenko, Reader J & NIST ASD Team 2020 NIST Atomic Spectra Database (ver. 5.8), [Online]. Available: `https://physics.nist.gov/asd` [2020, November 3]. National Institute of Standards and Technology, Gaithersburg, MD.
Kröll S & Bischel W K 1990 *Phys. Rev. A* **41**, 1340.
Lottigier P, Jucha A, Cabaret L, Blondel C & Drag C 2019 *Appl. Phys. B* **125**, 14.
Loy M M 1976 *Phys. Rev. Lett.* **36**, 1454.
Marchal F, Sewraj N, Jabbour G, Akerreta P R & Ledru G 2010 *J. Phys. B: At. Mol. Opt. Phys.* **43**, 235210.
Marinov D, Booth J P, Drag C & Blondel C 2017 *J. Phys. B: At. Mol. Opt. Phys.* **50**, 065003.
Matsuta H & Kitagawa K 2012 *Spectrosc. Lett.* **45**, 13.
McIlrath T, Hudson R, Aikin A & Wilkerson T 1979 *Appl. Optics* **18**, 316.
Meier U, Kohse-Hoinghaus K, Schafer L & Klages C P 1990 *Appl. Optics* **29**, 4993.
Milonni P & Eberly J 1978 *J. Chem. Phys.* **68**, 1602.
Niemi K, Schulz-Von Der Gathen V & Döbele H 2001 *J. Phys. D: Appl. Phys.* **34**, 2330.
Niemi K, Schulz-Von Der Gathen V & Döbele H 2005 *Plasma Sources Sci. Technol.* **14**, 375.
Pendleton S, Bowman S, Carter C, Gundersen M & Lempert W 2013 *J. Phys. D: Appl. Phys.* **46**, 305202.
Pindzola M, Payne M & Garrett W 1981 *Phys. Rev. A* **24**, 3115.
Pindzola M S 1978 *Phys. Rev. A* **17**, 1021.
Preppernau B L, Dolson D A, Gottscho R A & Miller T A 1989 *Plasma Chem. Plasma P.* **9**, 157.
Raymond T, Böwering N, Kuo C Y & Keto J 1984 *Phys. Rev. A* **29**, 721.
Rumi M & Perry J W 2010 *Adv. Opt. Photonics* **2**, 451.
Salah W & Hassouneh O 2019 *Results Phys.* **12**, 153.
Saxon R P & Eichler J 1986 *Phys. Rev. A* **34**, 199.
Schuller F & Behmenburg W 1974 *Phys. Rep.* **12**, 273.
Settersten T B & Linne M A 2002 *J. Opt. Soc. Am. B* **19**, 954.
Stancu G D 2020 *Plasma Sources Sci. Technol.* **29**, 054001.
Takatsuji M 1975 *Phys. Rev. A* **11**, 619.
Tiee J, Ferris M, Loge G & Wampler F 1983 *Chem. Phys. Lett.* **96**, 422.
Uddi M, Jiang N, Mintusov E, Adamovich I V & Lempert W R 2009 *P. Combust. Inst.* **32**, 929. (in

press).
Van der Heijden H, Boogaarts M, Mazouffre S, Van der Mullen J & Schram D 2000 *Phys. Rev. E* **61**, 4402.
van Gessel A F H, van Grootel S C & Bruggeman P J 2013 *Plasma Sources Sci. Technol.* **22**, 055010.
Vasilenko L S, Chebotaev V P & Shishaev A V 1970 *JETP Letters* **12**, 113 (161).
Walkup R, Saenger K & Selwyn G 1986 *J. Chem. Phys.* **84**, 2668.
Whitehead C, Cannon B & Wacker J 1995 *Appl. Optics* **34**, 3250.
Whitehead C, Pournasr H, Bruce M, Cai H, Kohel J, Layne W & Keto J W 1995 *J. Chem. Phys.* **102**, 1965.